Targetome

ORIGINAL ARTICLE

Open Access

https://doi.org/10.48130/targetome-0026-0055

Targetome **2026**, 2(6): e057

Dual targeting of MAPK8 and JAK2 as a host-directed anti-inflammatory strategy for severe *Klebsiella pneumoniae* infection

Yang Zhang[1#], Yanghao Lin[1#], Kangkang Luo[1#], Jingying Zhang[2#], Yu Li[1], Ronghui Du[1], Hongwei Yi[3*], Xiaomin Lu[2*] and Xudong Wu[1*]

[1] *State Key Laboratory of Pharmaceutical Biotechnology, School of Life Sciences, Nanjing University, No. 163 Xianlin Avenue, Nanjing 210023, China*
[2] *Jiangsu Province Hospital of Chinese Medicine, Affiliated Hospital of Nanjing University of Chinese Medicine, 155 Hanzhong Road, Nanjing 210004, China*
[3] *Department of Pharmacology, School of Medicine, Southeast University, No. 87 Dingjiaqiao, Nanjing 210009, China*
[#] Authors contributed equally: Yang Zhang, Yanghao Lin, Kangkang Luo, Jingying Zhang
* Correspondence: hwyi@seu.edu.cn (Yi H); xmlu78@126.com (Lu X); xudongwu@nju.edu.cn (Wu X)

Abstract

Severe *Klebsiella pneumoniae* empyema remains a therapeutic challenge because of complex host–pathogen interactions and frequent antibiotic failure. To dissect the underlying microenvironmental mechanisms and identify candidate therapeutics, we conducted a proof-of-concept single-patient study integrating longitudinal clinical multi-omics, single-cell spatial mapping, and virtual pharmacological screening. Untargeted metabolomics of pleural fluid revealed taurine-associated host-pathogen co-metabolism and identified a microbiota-specific reductase (K15373) as a computationally predicted metabolic vulnerability. Parallel transcriptomic network analysis identified a core signaling triad (MAPK8, JAK2, and TP53) associated with dysregulated inflammation, which was confirmed both in a *K. pneumoniae* lipopolysaccharide (LPS)-induced murine model of acute lung injury (ALI) and in longitudinal clinical pleural fluid samples. Projection of these targets onto a single-cell atlas of severe pulmonary infection revealed elevated expression in alveolar macrophages and type II pneumocytes, and a machine learning-based single-cell virtual knockout algorithm indicated that the hub genes contribute to cytokine release and epithelial barrier disruption. Network pharmacology and transcriptomic perturbation screening against large-scale databases then identified curcumin and evodiamine as candidate compounds that counteract the severe disease signature, and molecular dynamics simulations coupled with thermodynamic calculations predicted stable, high-affinity binding of curcumin to MAPK8 and of evodiamine to JAK2. We then evaluated the candidates *in vivo* in the *K. pneumoniae* LPS-induced murine ALI model. Given alone or in combination, curcumin and evodiamine attenuated body weight loss, pulmonary edema, alveolar-capillary barrier disruption, and histopathological injury. Western blot analysis showed that curcumin preferentially suppressed MAPK8/JNK phosphorylation, whereas evodiamine inhibited JAK2 phosphorylation, while combination therapy normalized both pathways; immunofluorescence revealed reduced infiltration of F4/80$^+$ macrophages and Ly6G$^+$ neutrophils. These results provide, to our knowledge, the first *in vivo* evidence that dual pharmacological inhibition of MAPK8 and JAK2 mitigates *K. pneumoniae* LPS-driven pulmonary inflammation. Overall, this computational systems biology approach characterizes the immunometabolic features of the infectious microenvironment and supports further medicinal chemistry optimization of curcumin- and evodiamine-based scaffolds as candidate dual-targeting agents, with particular attention to pharmacokinetic optimization and safety profiling.

Keywords: *Klebsiella pneumoniae* empyema, Multi-omics integration, MAPK8/JAK2 dual inhibition, Network pharmacology, Host-directed therapy

Citation: Zhang Y, Lin Y, Luo K, Zhang J, Li Y, et al. 2026. Dual targeting of MAPK8 and JAK2 as a host-directed anti-inflammatory strategy for severe *Klebsiella pneumoniae* infection. *Targetome* 2(6): e057 https://doi.org/10.48130/targetome-0026-0055

Introduction

Hypervirulent *Klebsiella pneumoniae* (HvKp) is an emerging pathogen that causes invasive infections, including pyogenic liver abscesses, necrotizing pneumonia, and empyema[1–4]. HvKp-associated empyema is characterized by accumulation of hypermucoviscous, loculated purulent fluid that responds poorly to chest tube drainage alone[5]. Within the pleural space, uncontrolled local inflammation and barrier disruption can progress to systemic sepsis[6], and mortality remains as high as 15%–30% despite appropriate antimicrobial therapy and surgical intervention[7,8]. The persistence of such poor outcomes indicates that conventional antibiotics aimed at pathogen clearance are insufficient in this setting and that modulating host–pathogen interactions may provide an additional therapeutic avenue; host-directed therapies (HDTs), which act on host pathways involved in infection-associated inflammation and tissue damage, have accordingly been proposed as adjuncts to antimicrobial treatment[9,10].

The pleural space in severe infection is a densely interconnected compartment in which host immune cells, resident epithelial barriers, and invading bacteria engage in continuous metabolic and transcriptional crosstalk[11]. Recent work has begun to resolve these interactions. *K. pneumoniae* was shown to impose metabolic stress on host pulmonary tissue, promoting tolerance to infection[12]; metabolomic profiling of parapneumonic effusions linked accumulated dipeptides to IL-8 production by neutrophilic cells[13]; and *in vivo* single-cell transcriptomics demonstrated that *K. pneumoniae* skews lung macrophages toward an M2-like, infection-permissive state through a TLR-type I interferon-IL-10-STAT6 axis[14]. These studies, however, have largely examined either the bacterial or the host compartment at a single disease stage, and an integrated, longitudinal characterization of the hvKp empyema microenvironment that links pathogen metabolism to host inflammatory signaling remains lacking.

Identifying therapeutics within such networks is complicated by functional redundancy among signaling pathways, which limits the efficacy of single-target interventions. Network pharmacology integrated with Traditional Chinese Medicine (TCM) offers a multi-target framework suited to the systems-level alterations of severe infection[15–17], and natural product-derived interventions,

© The Author(s)

including curcumin, have been shown to attenuate LPS-induced acute lung injury through coordinated anti-inflammatory and anti-ferroptosis mechanisms[18].

In this study, we investigated whether progression of severe hvKp empyema involves host–pathogen co-metabolic dependencies and key transcriptional regulatory nodes that can be exploited as targets for natural compounds. Three challenges had to be addressed: assigning molecular events in pleural fluid to host vs microbial sources; identifying druggable nodes within the resulting multi-layered networks; and moving from computational predictions to experimentally validated pharmacology. We therefore established an integrative framework that combines longitudinal clinical multi-omics profiling, single-cell spatial mapping, and machine learning-based virtual perturbation to nominate targets, followed by network pharmacology, molecular dynamics simulations, and *in vivo* pharmacological evaluation. Specifically, we tested curcumin, evodiamine, and their combination in a *K. pneumoniae* LPS-induced murine acute lung injury model and included selective inhibitors of MAPK8 (SP600125) and JAK2 (fedratinib) to dissect the individual and combined contributions of these kinases to pulmonary inflammation.

This work makes three contributions. First, it provides a longitudinal multi-omics characterization of the hvKp empyema microenvironment, including a taurine-associated host-pathogen co-metabolic circuit and a microbiota-specific reductase predicted to be a conditional metabolic vulnerability. Second, it identifies a host inflammatory hub network centered on *MAPK8*, *JAK2*, and *TP53*, maps its activation to alveolar macrophages and type II pneumocytes, and ranks hub-gene essentiality by single-cell virtual knockout. Third, it translates this network into candidate dual-targeting compounds, with curcumin targeting MAPK8 and evodiamine targeting JAK2, and provides *in vivo* evidence from an LPS-induced lung injury model that combined inhibition of both kinases attenuates pulmonary inflammation. In doing so, it offers a transferable computational-experimental framework for developing host-directed therapies against refractory pulmonary infections.

Materials and methods

Patient cohort and ethical approval

A patient diagnosed with hypervirulent *K. pneumoniae* empyema was enrolled at the Jiangsu Province Hospital of Chinese Medicine (Affiliated Hospital of Nanjing University of Chinese Medicine, Nanjing, China). The diagnosis was confirmed by pleural fluid culture and metagenomic next-generation sequencing (mNGS), which identified *K. pneumoniae* as the dominant pathogen with detection of virulence genes (*iutA*, *rmpA*)[19] alongside the extended-spectrum β-lactamase gene *blaSHV*. Pleural fluid samples were collected longitudinally at three time points (weeks 1, 2, and 3) of the clinical course for multi-omics profiling, including untargeted metabolomics and bulk RNA sequencing. Written informed consent was obtained from the patient prior to sample collection. This investigator-initiated clinical research was approved by the Ethics Committee of the Affiliated Hospital of Nanjing University of Chinese Medicine (Jiangsu Province Hospital of Chinese Medicine; Approval No. 2025NL-025-02, approved on February 8, 2025). All procedures were conducted in accordance with the Declaration of Helsinki and the International Ethical Guidelines for Health-related Research Involving Humans issued by CIOMS.

ELISA measurement of pleural fluid cytokines

Pleural fluid supernatants were separated by centrifugation (3,000 × *g*, 10 min, 4 °C) and stored at −80 °C until analysis. Cytokine concentrations in pleural fluid supernatants were quantified using commercial ELISA kits according to the manufacturers' instructions, including IL-6 (Human IL-6 ELISA Kit, ExCell Biology, Cat#EH004-48), IL-8 (Human IL-8 ELISA Kit, HuaAn Biotechnology, Cat#EH0014), IL-10 (Human IL-10 ELISA Kit, ExCell Biology, Cat#EH006-48), IL-1β (Human IL-1β ELISA Kit, Abclonal, Cat#RK00001), and TGF-β1 (Human TGF-β1 ELISA Kit, HuaAn Biotechnology, Cat#EH0012). All measurements were performed in duplicate.

Untargeted metabolomics profiling

Pleural fluid cell pellets were extracted using methanol : water (4 : 1, *V/V*) for hydrophilic metabolites and methyl tert-butyl ether : methanol (3 : 1, *V/V*) for lipids, followed by three freeze-thaw cycles (liquid nitrogen/dry ice) and centrifugation. Metabolite profiling was performed on an ExionLC AD UPLC system coupled to a QTRAP 6500 mass spectrometer (SCIEX) operating in multiple reaction monitoring (MRM) mode with electrospray ionization (ESI). Hydrophilic metabolites were separated on a Waters HSS T3 C18 column (1.8 μm, 2.1 mm × 100 mm); lipids on a Thermo Accucore C30 column (2.6 μm, 2.1 mm × 100 mm). Metabolites were identified by matching retention times and MS/MS spectra against the Metware Database (MWDB). Pooled quality control (QC) samples were analyzed throughout each batch, and data were normalized by BCA protein concentration. Differential metabolites were selected based on $|\log_2$ fold change$| \geq 1$, variable importance in projection (VIP) ≥ 1 from OPLS-DA models (R2Y/Q2 ≥ 0.5), and FDR-adjusted $P < 0.05$. Pathway enrichment analysis was conducted *via* MetaboAnalyst 5.0[20]. The dataset has been deposited in MetaboLights under accession MTBLS14738. Microbial origin assignment of metabolites was performed using MetOrigin (v2.0; http://metorigin.met-bioinformatics.cn/), which maps metabolites to their biological sources (host, microbiota, or co-metabolism) based on integrated KEGG and HMDB pathway annotations with a confidence score threshold of ≥ 0.5.

Bulk RNA sequencing and transcriptomic analysis

Total RNA was extracted from pleural fluid cell pellets using TRIzol (Invitrogen). RNA quality and integrity were assessed using a Qubit 4.0 fluorometer and Qsep400 bioanalyzer (RIN > 7.0 required). Polyadenylated mRNA was enriched using Oligo(dT) magnetic beads, fragmented, and reverse-transcribed into cDNA. Sequencing libraries were constructed *via* end repair, A-tailing, adapter ligation, and PCR enrichment, then sequenced on an Illumina platform using sequencing-by-synthesis (SBS) chemistry (three samples; approximately 24.48 Gb of clean data, Q30 ≥ 94%). Raw reads were quality-filtered with fastp (v0.23.2) and aligned to the GRCh38 human reference genome using HISAT2 (v2.2.1). Gene-level expression quantification was performed with featureCounts (v2.0.3). Differential expression analysis was conducted using DESeq2 (v1.38.3) and edgeR (v3.40.2), with significance thresholds of $|\log_2$ fold change$| \geq 1$ and adjusted $P < 0.05$ (Benjamini–Hochberg FDR). Functional enrichment analysis (GO, KEGG, Reactome, GSEA) was performed using clusterProfiler (v4.6.0). The raw sequencing data have been deposited in the NCBI Sequence Read Archive (SRA) under BioProject PRJNA1476439.

Public single-cell and bulk transcriptomic data processing

Public single-cell and bulk transcriptomic datasets were retrieved from the Gene Expression Omnibus (GEO) repository and explored interactively *via* the CZI CellxGene data portal. Three independent cohorts were analyzed: GSE171524 (snRNA-seq of frozen lung tissue from 19 fatal COVID-19 cases and seven non-COVID controls; 116,314 nuclei across 27 samples), GSE158055 (scRNA-seq of bronchoalveolar lavage fluid immune cells from 196 individuals spanning mild, severe, and convalescent COVID-19 phases; 284 samples), and GSE76293 (Affymetrix microarray profiling of blood and alveolar neutrophils from 12 ARDS patients and 12 matched healthy controls; 94 samples). Quality control, dimensionality reduction, clustering, and cell-type annotation for sc/snRNA-seq data were performed through the CellxGene online analysis environment. Gene set enrichment analysis (GSEA) against MSigDB Hallmark gene sets was computed using the Microbioinformatics (Weishengxin) platform. Virtual knockout screening was conducted using scTenifoldKnk[21] (v1.2.0) to infer gene essentiality through regulatory network perturbation[22].

Network pharmacology screening

Nine hub genes were queried against HERB 2.0[23] for compound-target interactions; compounds targeting two or more hub genes were prioritized. SwissTargetPrediction and BindingDB supplemented target prediction. A bipartite compound-gene network was constructed in Cytoscape[24] to visualize convergence patterns.

Molecular docking and dynamics simulations

MAPK8 (PDB: 4QTD) and JAK2 (PDB: 8BXH) structures were retrieved from the RCSB PDB. Curcumin (PubChem CID 969516) and evodiamine (CID 442088) were docked *via* the CB-DOCK2[25] web server with PyMOL visualization. MD simulations used GROMACS 2022.2; ligand topologies were generated by CGenFF[26], and the CHARMM36 force field was employed for proteins[27]. A 100 ns production run was followed by energy minimization and equilibration (NVT/NPT ensembles, 310 K, 1 bar).

Animal experiments

All animal experiments were performed in strict accordance with the NIH Guide for the Care and Use of Laboratory Animals and the ARRIVE guidelines. The experimental protocols were reviewed and approved by the Institutional Animal Care and Use Committee (IACUC) of Nanjing University (Approval No. IACUC2410004).

Male C57BL/6J mice (8–10 weeks old; GemPharmatech Co., Ltd, Nanjing, China) were housed under SPF conditions and randomly assigned to Control (n = 6, intratracheal sterile PBS) and LPS model groups (n = 20). Acute lung injury was induced by single intratracheal instillation of *K. pneumoniae*-derived LPS (Sigma-Aldrich, Cat#L4268, 300 μg/mouse) under anesthesia with analgesia (day 0). At each time point, mice were randomly selected for euthanasia: day 1 (n = 5–6) and day 3 (n = 5–6), with the remaining animals monitored for survival analysis.

Pharmacological evaluation experiments

Curcumin (purity ≥ 98%, Macklin, Cat#C805205) and evodiamine (purity ≥ 98%, Macklin, Cat#E665354) were dissolved in 0.5% carboxymethylcellulose sodium (CMC-Na) and administered by oral gavage once daily. SP600125 (MCE, Cat#HY-12041)[28] was dissolved in 2% DMSO + 30% PEG300 + 5% Tween 80 + ddH_2O and administered by intraperitoneal injection. Fedratinib (MCE, Cat#HY-10409)[29] was dissolved in 0.5% CMC-Na and administered by oral gavage. *K. pneumoniae*-derived LPS (Sigma-Aldrich, Cat#L4268, 100 μg/mouse) was delivered by intratracheal instillation on day 0 under isoflurane anesthesia, 1 h after the first drug dose. Treatment continued once daily until sacrifice at 72 h.

For the natural product efficacy experiment, C57BL/6J mice were randomly assigned to seven groups: Control (sterile PBS + vehicle, n = 4); Model (Kp-LPS + vehicle, n = 12); Cur-L (Kp-LPS + curcumin 50 mg·kg^{-1}, n = 5); Cur-H (Kp-LPS + curcumin 200 mg·kg^{-1}, n = 6); Evo-L (Kp-LPS + evodiamine 10 mg·kg^{-1}, n = 5); Evo-H (Kp-LPS + evodiamine 40 mg·kg^{-1}, n = 6); and Combo (Kp-LPS + Cur-H + Evo-H, n = 10). For the inhibitor validation experiment, mice were assigned to five groups: Control, Model, MAPK8i (Kp-LPS + SP600125 15 mg·kg^{-1}, i.p., n = 5), JAK2i (Kp-LPS + fedratinib 30 mg·kg^{-1}, i.g., n = 5), and Dual-i (Kp-LPS + SP600125 + fedratinib, n = 5).

Bronchoalveolar lavage fluid (BALF) was collected *via* tracheal cannulation with 0.8 mL ice-cold PBS (× 3). Total protein concentration in BALF supernatant was measured using a BCA Protein Assay Kit (Beyotime, Cat#P0010). Left lung lobes were fixed in 4% paraformaldehyde, paraffin-embedded, and sectioned at 5 μm for H&E and Masson's trichrome staining. Lung injury was scored by a blinded pathologist on a 0–10 scale evaluating alveolar congestion, hemorrhage, neutrophil infiltration, and alveolar wall thickening. Collagen area (%) was quantified from Masson's trichrome images using ImageJ (NIH).

For western blot, right lung tissues were homogenized in RIPA buffer with protease and phosphatase inhibitors. Lysates (30 μg/lane) were resolved on 6% and 12% SDS-PAGE gels (corresponding to the molecular weights of the target proteins) and transferred to PVDF membranes (Millipore). Primary antibodies: anti-phospho-JNK (Thr183/Tyr185, 1 : 1,000, Proteintech, Cat#60666-1-Ig), anti-MAPK8 (1 : 1,000, Biodragon, Cat#BD-PB2521), anti-phospho-JAK2 (Tyr1007/1008, 1 : 1,000, Selleck, Cat#F4153), anti-JAK2 (1 : 1,000, Affinity, Cat#AF6023), and anti-β-actin (1 : 10,000, Affinity, Cat#AF7018). HRP-conjugated secondary antibodies and ECL detection were used, and bands were quantified with ImageJ.

For immunofluorescence, deparaffinized lung sections underwent antigen retrieval and were co-incubated with anti-F4/80 (1 : 200, Servicebio, Cat#GB113373) and anti-Ly6G (1 : 200, Servicebio, Cat#GB11229) overnight at 4 °C, followed by Alexa Fluor 488- and Cy3-conjugated secondary antibodies. Nuclei were counterstained with DAPI. Serum IL-1β, TNF-α, and TGF-β1 levels were quantified using commercial ELISA kits per the manufacturers' instructions.

Cellular thermal shift assay (CETSA)

A549 cells were cultured in DMEM supplemented with 10% fetal bovine serum at 37 °C under 5% CO_2. Cells were treated with DMSO (vehicle), curcumin (40 μmol·L^{-1}), or evodiamine (40 μmol·L^{-1}) for 3 h, then harvested and resuspended in PBS. Cell suspensions were aliquoted into PCR tubes and heated at 37, 43, 47, 50, 53, 56, 60, and 63 °C for 3 min in a gradient thermocycler, followed by immediate cooling on ice. Cells were lysed in PBS containing 0.4% NP-40 and a protease inhibitor cocktail by three freeze-thaw cycles, and soluble fractions were collected after centrifugation (12,000 × g, 10 min, 4 °C). MAPK8 and JAK2 in the soluble fractions were detected by western blot as described in Section *Pharmacological evaluation experiments*. Band intensities (integrated density) were quantified with ImageJ after local background subtraction and normalized to the corresponding 37 °C value. Melt curves were fitted to a four-parameter logistic model using GraphPad Prism (v10.1.2), with the plateaus fixed at 100% (37 °C) and 0% (fully denatured); the

apparent melting temperature (T_m) was defined as the inflection point of the fitted curve, and ΔT_m was calculated as the T_m shift relative to the DMSO group[30,31].

Statistical analysis

Data are expressed as mean ± standard error of the mean (SEM). Homogeneity of variance was first assessed. The independent-samples t-test and one-way analysis of variance (ANOVA) were used for comparisons between two groups and among three or more groups, respectively. In one-way ANOVA, the Tukey test was used for post-hoc multiple comparisons when variances were homogeneous, and the Games–Howell method was used when variances were heterogeneous. Body weight and food intake time-course data were analyzed by two-way repeated-measures ANOVA. Survival data were analyzed by the Kaplan–Meier method, and survival curves were compared by the log-rank test. The Mann–Whitney U test and Kruskal–Wallis test were applied to histological scores between two groups and among three or more groups, respectively. For phosphorylation analyses, the phospho-to-total protein ratio was used as the primary endpoint, with drug-treated groups compared against the LPS (Model) group; total protein expression was normalized to β-actin and compared against the Control group. For transcriptomic and metabolomic data, differential analyses were performed in R software (v4.4.1), Spearman correlation was used for correlation analysis, and P values for multiple comparisons were adjusted using the Benjamini–Hochberg false discovery rate (FDR). Statistical analyses were performed using GraphPad Prism (v10.1.2) and R software (v4.4.1). A two-tailed $P < 0.05$ was considered statistically significant, and specific P values are marked in the figures.

Results

Longitudinal metabolomic profiling identifies host lipid remodeling and microbiota-associated taurine metabolism signatures in hvKp empyema

To delineate the microenvironmental evolution during severe infection, we prospectively evaluated a 61-year-old male patient diagnosed with hypervirulent *K. pneumoniae* (hvKp) empyema complicated by septic shock. Metagenomic next-generation sequencing (mNGS) of the pleural fluid confirmed hvKp as the absolute dominant pathogen (92.3% relative abundance). The strain harbored classical hypervirulence factors (*iutA, rmpA*)[19], and the extended-spectrum β-lactamase (ESBL) resistance gene *blaSHV* (Supplementary Table S1). Pleural fluid samples were collected longitudinally at weekly intervals (week 1 to week 3) until clinical resolution. Supernatants were subjected to ELISA-based cytokine profiling, while cell pellets were reserved for untargeted metabolomic and bulk RNA-sequencing analyses (Fig. 1a).

Radiographic follow-up by chest CT at weeks 1, 3, 11, and 76 demonstrated progressive resolution of pleural effusion and parenchymal consolidation (Fig. 1b). Clinical inflammatory markers including C-reactive protein (CRP), neutrophil percentage, and neutrophil-to-lymphocyte ratio (NLR) all peaked at week 2 and declined to their lowest levels by week 3 (Fig. 1c). Consistent with the resolution of acute infection, levels of pro-inflammatory IL-1β and the regulatory cytokine IL-10 steadily declined from week 1 to week 3. Conversely, tissue repair-associated mediators TGF-β1 and IL-6 exhibited an initial drop followed by a marked rebound in the late phase, while the neutrophil chemoattractant IL-8 displayed a continuous rise (Fig. 1d). These dynamic patterns indicate a microenvironmental transition from acute inflammatory stress toward active tissue remodeling and sustained chemotaxis.

A total of 1,400 differential metabolites were quantified and subjected to K-means clustering, partitioning into eight temporal clusters (C1–C8) with divergent kinetic trajectories (Fig. 1e). Global superclass composition analysis identified glycerophospholipids (GP, ~35%) and sphingolipids (SP) as the most abundant chemical classes, followed by amino acids and derivatives, fatty acyls, and glycerolipids (Fig. 1f). The proportional distribution of these superclasses varied substantially across clusters (Fig. 1g and h). In dynamic clusters C6 and C7, which peaked during the severe symptomatic phase (week 2), and in C3 and C4, which showed marked elevation during the resolution phase (week 3), GPs consistently ranked as the predominant metabolite class, with SPs constituting the second most abundant category.

MetOrigin-based source assignment classified the metabolites into host-derived (n = 920), microbiota-derived (n = 782), and host-microbiota co-metabolism products (n = 707) (Fig. 1i). Pathway enrichment analysis stratified by biological origin revealed that host-derived metabolites were significantly enriched in arachidonic acid, glycerophospholipid, and sphingolipid metabolism (Fig. 1j). In-depth profiling of GP and SP subclasses indicated a distinct lipid class shift from PG/PI and CER to PE/SM as the disease resolved (Fig. 1k and l).

In contrast, microbiota-associated pathway enrichment strikingly converged on taurine and hypotaurine metabolism as the most significantly altered pathway. Detailed interrogation of the taurine metabolic axis identified 2-hydroxyethanesulfonate as a microbiota-specific signature metabolite. Metabolic network reconstruction revealed a crucial host-pathogen co-metabolic circuit: *K. pneumoniae* exploits a bacteria-restricted sulfoacetaldehyde reductase (EC 1.1.1.313, encoded by the K15373 gene) to catalyze the NADH-dependent reduction of host-generated toxic sulfoacetaldehyde into 2-hydroxyethanesulfonate (Fig. 1m and n). Sequence alignment confirmed the absence of homologous sequences in the human genome (Identity < 35%) (Fig. 1o).

To assess the potential metabolic essentiality of this enzyme, we performed flux balance analysis (FBA) using a genome-scale metabolic model (GSMM) of *K. pneumoniae*. The topological network highlighted K15373 as a central detoxification hub (Supplementary Fig. S1a and S1b). *In silico* knockout of K15373 (ΔK15373) had negligible effects on bacterial growth in complete media, whereas it abolished the predicted biomass flux under simulated pleural fluid conditions (hypoxia and nutrient restriction; Supplementary Fig. S1c). This computational evidence predicts K15373 reductase as a conditional survival vulnerability in the empyema microenvironment, pending genetic validation.

Transcriptomic dynamics in the empyema microenvironment identify a nine-gene hub network driving inflammatory and metabolic remodeling

Parallel bulk transcriptomic profiling of pleural fluid cell pellets captured temporal gene expression dynamics across the same 3-week clinical interval. Mfuzz soft clustering partitioned 6,015 differentially expressed genes into five distinct temporal clusters (C1–C5) with divergent expression trajectories (Fig. 2a). Gene Ontology (GO) and KEGG enrichment analyses stratified by phase revealed distinct biological transitions: the early-phase clusters (C2 + C4) were predominantly associated with lipid remodeling and energy metabolism (e.g., oxidative phosphorylation, ATP metabolic processes); the mid-phase cluster (C1) reflected a robust acute inflammatory response driven by neutrophil extracellular trap (NET)

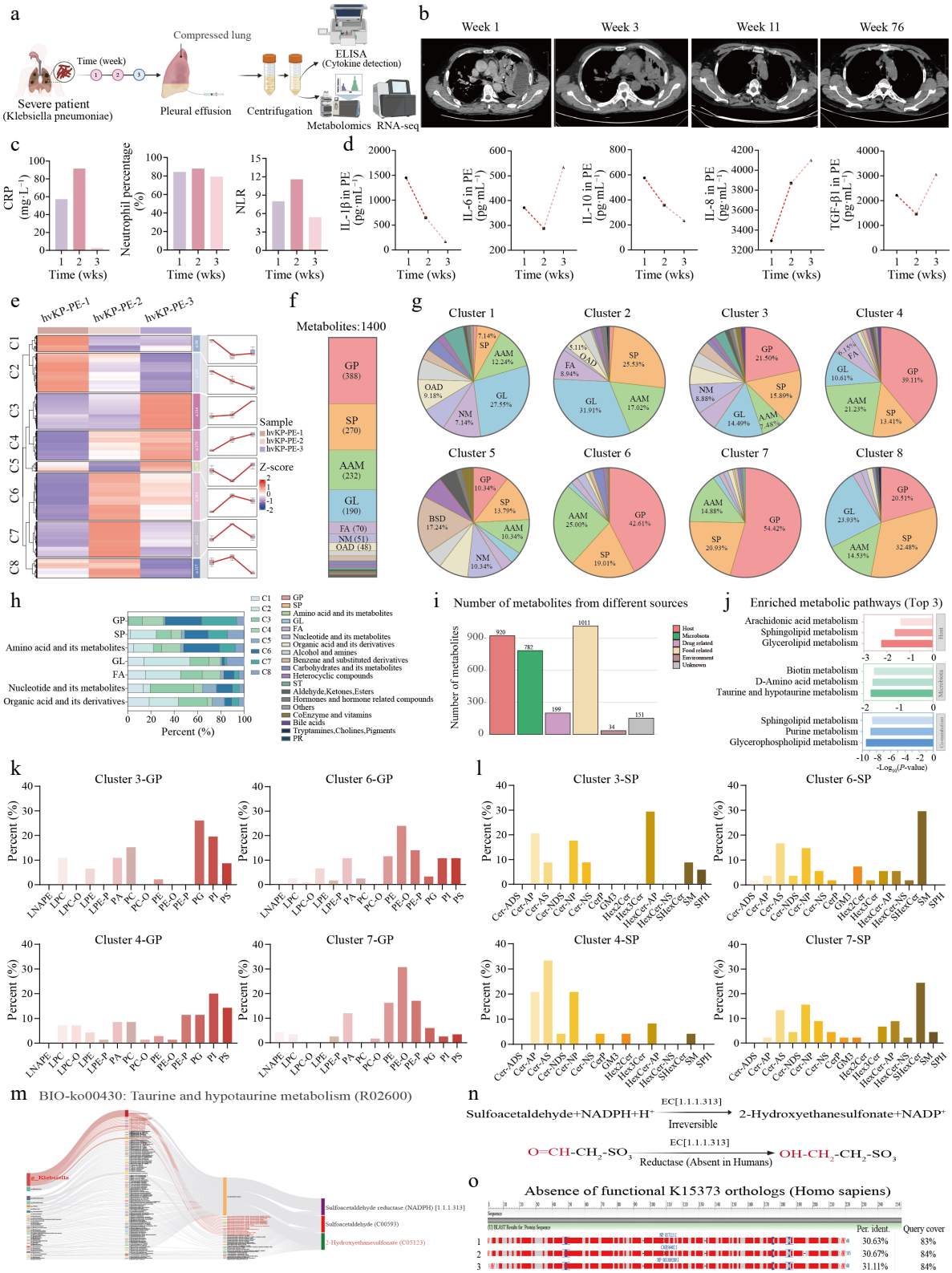


Fig. 1 Longitudinal untargeted metabolomic profiling identifies taurine-driven host-microbiota co-metabolism as a hallmark signature of *Klebsiella pneumoniae* empyema. (a) Schematic overview of the study design and analytical workflow. (b) Representative chest CT scans at weeks 1, 3, 11, and 76. (c) Temporal profiles of CRP, neutrophil percentage, and NLR. (d) ELISA quantification of five cytokines (IL-1β, IL-6, IL-10, IL-8, TGF-β1) in pleural fluid across three time points. (e) K-means clustering heatmap of differential metabolites partitioned into eight temporal clusters (C1–C8), with centroid trajectory line plots. (f) Superclass composition of all identified metabolites. (g) Pie charts of superclass composition within each cluster (clusters 1–8). (h) Stacked bar chart of cluster contribution to each superclass. (i) MetOrigin-based assignment of metabolites by biological source. (j) KEGG pathway enrichment analysis (Top 3) stratified by metabolite source. Subclass composition within selected temporal clusters: (k) glycerophospholipid (GP) subclasses; and (l) sphingolipid (SP) subclasses. (m) KEGG pathway map (map00430) of taurine and hypotaurine metabolism. (n) Catalytic reaction of bacterial sulfoacetaldehyde reductase. (o) BLASTp alignment demonstrating the absence of functional K15373 orthologs in the human genome.

https://doi.org/10.48130/targetome-0026-0055

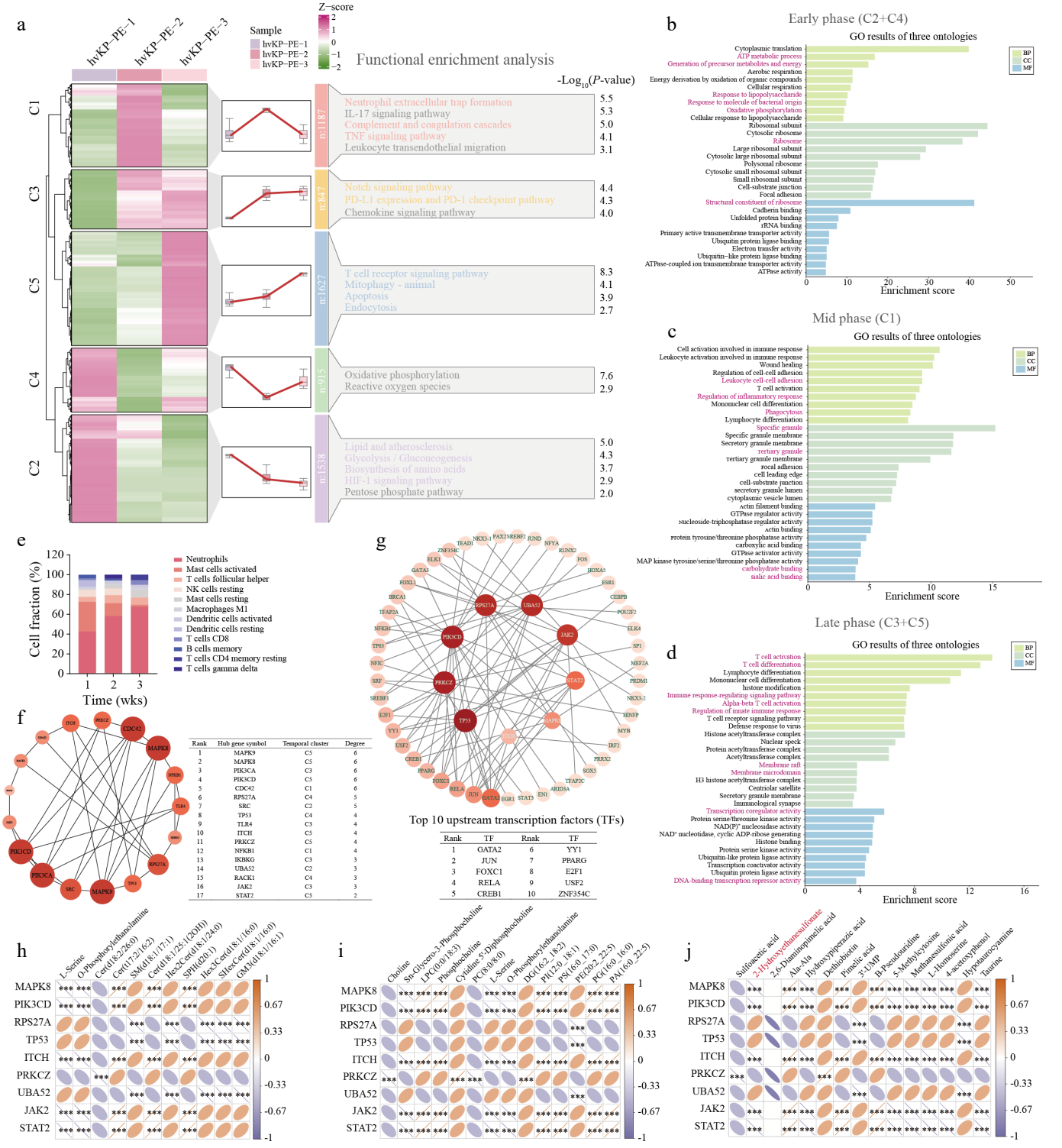


Fig. 2 Transcriptomic dynamics in the empyema microenvironment identify a nine-gene hub network driving inflammatory and metabolic remodeling. (a) Mfuzz temporal clustering heatmap displaying Z-score-normalized gene expression. Top 10 enriched gene ontology (GO) terms across biological process (BP), cellular component (CC), and molecular function (MF) categories for the (b) early phase (clusters C2 + C4), (c) mid phase (cluster C1), and (d) late phase (clusters C3 + C5). (e) Stacked bar chart depicting relative fractions of immune cell subpopulations inferred by CIBERSORTx across three time points. (f) PPI subnetwork diagram of phenotype-associated genes with an accompanying table listing top 17 hub genes ranked by betweenness centrality (degree threshold ≥ 2). (g) Upstream transcription factor (TF) regulatory network constructed *via* NetworkAnalyst, depicting predicted master regulators and their target hub genes. Spearman correlation matrices linking the expression of nine core hub genes with temporal abundances of (h) SPs, (i) GPs, and (j) microbiota/taurine-related metabolites. Color scales indicate positive (orange) and negative (blue) correlations. Statistical significance thresholds: $P < 0.05$; $P < 0.01$; $P < 0.001$.

formation and IL-17/TNF signaling; whereas the late-phase clusters (C3 + C5) were highly enriched for adaptive immune activation (e.g., T cell receptor signaling) and resolution pathways (Fig. 2b–d).

CIBERSORTx-based[32] deconvolution tracked compositional shifts in immune cell populations across the clinical course (Fig. 2e). The analysis revealed a persistent and progressively increasing

neutrophilic infiltration from week 1 through week 3, underscoring the hallmark purulent nature of the empyema microenvironment. Concurrently, adaptive and restorative immune populations, including M1 macrophages and specific T cell subsets, progressively emerged by week 3, corroborating the late-phase transcriptomic activation of T cell receptor signaling pathways.

To identify master regulators dictating this microenvironmental shift, a protein–protein interaction (PPI) network was constructed using STRING. Betweenness centrality analysis prioritized 17 candidate hub genes (Fig. 2f). Further refinement isolated a core nine-gene signature. Genes were selected by three criteria: (i) betweenness centrality within the top 15%, (ii) significant differential expression at two or more time points ($|\log_2 FC| \geq 1$, FDR < 0.05), and (iii) known relevance to inflammatory signaling or tissue remodeling. *MAPK8*, *JAK2*, and *TP53* emerged as the primary signaling drivers. Upstream transcription factor network inference *via* NetworkAnalyst predicted master regulators *GATA2* and *JUN* governing this hub network (Fig. 2g). To rigorously assess the generalizability and clinical diagnostic value of this nine-gene signature beyond our index patient, we performed cross-validation using an independent, large-scale severe pulmonary inflammation cohort (GSE76293). All nine core hub genes exhibited significant differential expression in ARDS patients compared to controls (Supplementary Fig. S2a). Receiver operating characteristic (ROC) analysis confirmed their exceptional discriminative performance, with the signaling triad (*MAPK8*, *JAK2*, *TP53*) yielding high diagnostic accuracies (AUC > 0.79, $P < 0.05$) (Supplementary Fig. S2b). Furthermore, correlation mapping within this external cohort corroborated that *MAPK8* and *JAK2* tightly governed specific immune cell infiltrations, showing significant positive correlations with hyper-activated adaptive immune subsets (Supplementary Fig. S2c). This cross-disease validation suggests that the identified hub network may represent a shared inflammatory vulnerability across diverse severe pulmonary conditions; validation in independent hvKp empyema cohorts is therefore required.

Cross-omics integration *via* pairwise Spearman correlation analysis associated these nine prioritized host hub genes with key metabolite classes from the longitudinal metabolomic dataset. Correlation matrices revealed that the nine hub genes exhibited significant associations with structural sphingolipids (Fig. 2h), glycerophospholipids (Fig. 2i), and microbiota-derived taurine-related metabolites (Fig. 2j), establishing multi-layered molecular connectivity between the host inflammatory hub network and pathogen-driven metabolic dysregulation.

In vivo characterization of *Klebsiella pneumoniae* LPS-induced severe pulmonary inflammation and experimental validation of hub gene dynamics

To evaluate the physiological relevance of the identified nine hub genes in the context of hvKp-driven pulmonary pathology, we established a murine model of acute lung injury (ALI) induced by intratracheal instillation of *K. pneumoniae* LPS in C57BL/6J mice (Fig. 3a). LPS-challenged animals exhibited significantly impaired survival compared to PBS-treated controls, accompanied by progressive body weight loss and reduced daily food intake over the 3-d observation period (Fig. 3b–d). The lung dry-to-wet weight ratio (D/W %) decreased significantly at day 1 and day 3 post-instillation relative to controls (Fig. 3e), indicating substantial fluid accumulation and severe alveolar-capillary barrier disruption.

Serum cytokine profiling by ELISA showed a highly dynamic, biphasic systemic immunological response (Fig. 3f). Day 1 was marked by an intense acute inflammatory storm, manifested as sharply elevated circulating levels of the canonical pro-inflammatory triad (IL-1β, IL-6, TNF-α) together with the counter-regulatory cytokine IL-10. By day 3, these acute-phase mediators had markedly receded, whereas TGF-β1, the master regulator of tissue remodeling and fibrogenesis, increased markedly. This systemic cytokine shift was tightly coupled to the localized histopathological progression in the lung (Fig. 3g). H&E staining confirmed severe acute parenchymal injury at day 1, distinguished by dense inflammatory infiltrate and frank alveolar architectural disruption. Masson's trichrome staining at day 3, in turn, documented progressive interstitial collagen deposition, thereby histologically corroborating the swift fibrotic transition driven by TGF-β1 upregulation (Fig. 3h).

To experimentally validate the multi-omics-derived nine-gene hub network, RT-qPCR quantification was conducted across both the *K. pneumoniae* LPS model and longitudinal clinical specimens (Supplementary Table S2). The transcriptional dynamics observed *in vivo* largely tracked the multiphasic pathological progression. In the murine model (Fig. 3i), acute stress-response nodes, notably *Trp53*, reached maximal expression at day 1 during the initial infectious insult. By contrast, key signaling kinases governing sustained inflammation and tissue remodeling, particularly *Mapk8* and *Jak2*, showed progressive upregulation that extended through day 3.

This temporal pattern was reproduced in longitudinal RT-qPCR analysis of the patient's pleural fluid cells over 3 weeks (Fig. 3j), aligning with local cytokine dynamics. Early-peaking genes tracked the acute IL-1β/IL-6 surge at week 1, whereas sustained *MAPK8*/*JAK2* upregulation by week 3 coincided with late-phase TGF-β1 and IL-8 elevation. This cross-species, cross-omics convergence identifies *MAPK8* and *JAK2* as central drivers of the inflammatory-to-fibrotic transition, highlighting their therapeutic relevance.

Single-cell mapping unveils dual-compartment hub gene activation under severe pulmonary infectious stress

To map the cell-type-specific expression and spatial distribution of the nine-gene hub network within the pulmonary microenvironment, we analyzed publicly available single-cell transcriptomic data spanning normal, pneumonia, and severe COVID-19 conditions[33,34].

Cell fraction analysis compared normal and severe infectious states and revealed compositional changes in the pulmonary immune landscape (Fig. 4a). Resident alveolar macrophages and type II pneumocytes decreased significantly under infectious stress, whereas adaptive immune populations expanded, consistent with immune recruitment. A dot plot quantified the expression of seven regulatory hub genes, excluding ubiquitous housekeeping genes, across the three conditions (Fig. 4b). Unsupervised clustering and UMAP projection resolved distinct pulmonary cell populations with unbiased annotation (Fig. 4c). Feature plots visualized these expression patterns within alveolar macrophages (Fig. 4d) and type II pneumocytes (Fig. 4e). *MAPK8* and *JAK2* showed cell-type-specific expression at moderate abundance, unlike the pan-cellular, high-abundance housekeeping genes. Alveolar macrophages and type II pneumocytes therefore represent the primary cellular compartments expressing the pathogenic hub genes during infectious stress.

Gene set enrichment analysis (GSEA) against MSigDB Hallmark gene sets was applied to the transcriptional signature of alveolar macrophages under severe infectious stress (Fig. 4f and g). The P53 and PI3K/AKT/mTOR pathways were significantly upregulated, along with the interferon-gamma response and hypoxia-related pathways. Alveolar macrophages thus mediate pro-apoptotic surveillance and metabolic reprogramming in response to infection. GSEA of type II

https://doi.org/10.48130/targetome-0026-0055

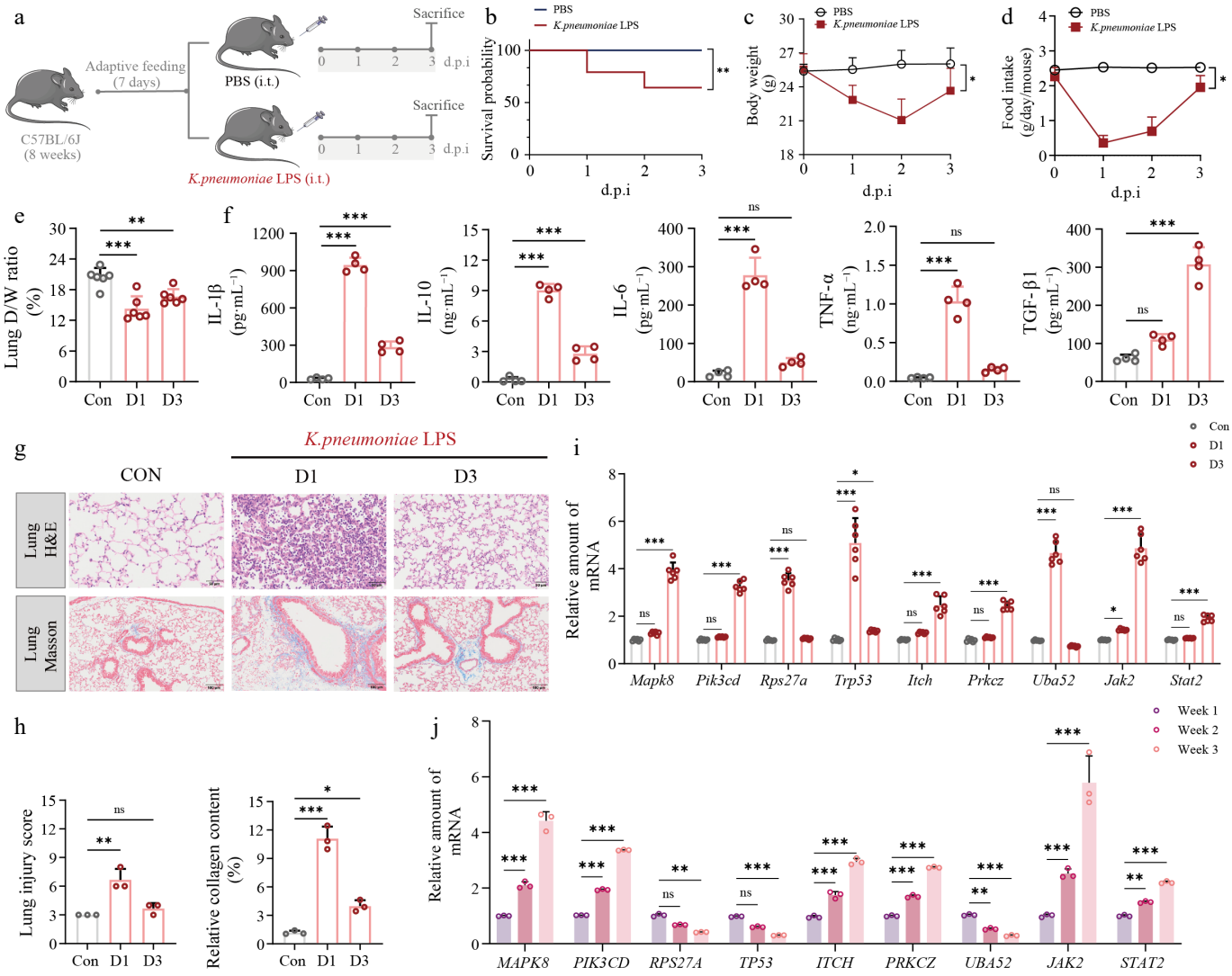


Fig. 3 *In vivo* characterization of *K. pneumoniae* LPS-induced severe pulmonary inflammation and experimental validation of hub gene dynamics. (a) Schematic diagram; (b) Kaplan–Meier survival curves; (c) body weight; (d) daily food intake over 3 d post-instillation; (e) lung dry/wet mass fraction (D/W%); (f) ELISA quantification of five cytokines (IL-1β, IL-10, IL-6, TNF-α, TGF-β1) in serum. (g), (h) Representative H&E (upper panel) and Masson trichrome (lower panel) images of lung tissue sections. Scale bars: 50 μm (H&E) and 100 μm (Masson). (i) RT-qPCR quantification of nine hub gene mRNA expression levels (*Mapk8, Pik3cd, Rps27a, Trp53, Itch, Prkcz, Uba52, Jak2, Stat2*) in mouse lung tissues across Control, day 1, and day 3 groups, $n = 6$. (j) Clinical RT-qPCR validation tracking mRNA expression dynamics of the corresponding human orthologs (*MAPK8, PIK3CD, RPS27A, TP53, ITCH, PRKCZ, UBA52, JAK2, STAT2*) in patient pleural fluid cells over the 3-week clinical course, $n = 3$. Data are presented as mean ± SD. Statistical significance: $P < 0.05$; $P < 0.01$; $P < 0.001$ vs Control; ns, not significant.

pneumocytes revealed distinct pathway alterations (Fig. 4h and i). GO Biological Process and KEGG analyses showed significant activation of the ER stress response, antigen processing and presentation, and EGF/EGFR-mediated actin signaling. These alterations indicate structural and functional impairment of the alveolar epithelial barrier. The pronounced ER stress response suggests that type II pneumocytes, the primary surfactant-producing and regenerative cells of the alveolus, undergo proteotoxic and metabolic strain. This strain, together with cytoskeletal remodeling, contributes to barrier disruption.

In silico single-cell virtual knockout screening reveals the pathogenic essentiality and regulatory landscape of hub genes

To link individual hub genes to the severe infectious transcriptional program observed across multiple omics layers, we applied an *in silico* virtual knockout (vKO) strategy using the machine-learning-based scTenifoldKnk algorithm[21] (Fig. 5a). The analysis used an independent single-cell transcriptomic dataset of bronchoalveolar lavage fluid (BALF) (GSE158055), including patients with severe pulmonary infection ($n = 9$) and mild cases ($n = 3$).

Global network disruption was quantified as the number of significantly dysregulated downstream genes after virtual deletion of each hub gene. This revealed cell-type-specific and severity-dependent perturbation patterns (Fig. 5b–d). In severe alveolar macrophages, virtual knockout of *STAT2*, *JAK2*, and *TP53* caused the largest downstream transcriptional changes, marking them as master inflammatory drivers. In alveolar epithelial cells and severe neutrophils, structural and housekeeping nodes such as *RPS27A* and *UBA52*, together with the signaling kinase *PRKCZ*, had the highest impact and caused profound network-wide collapse upon deletion (Fig. 5c and d).

GO pathway analysis characterized the functional consequences of the vKO-induced transcriptional changes (Fig. 5e and f). In severe

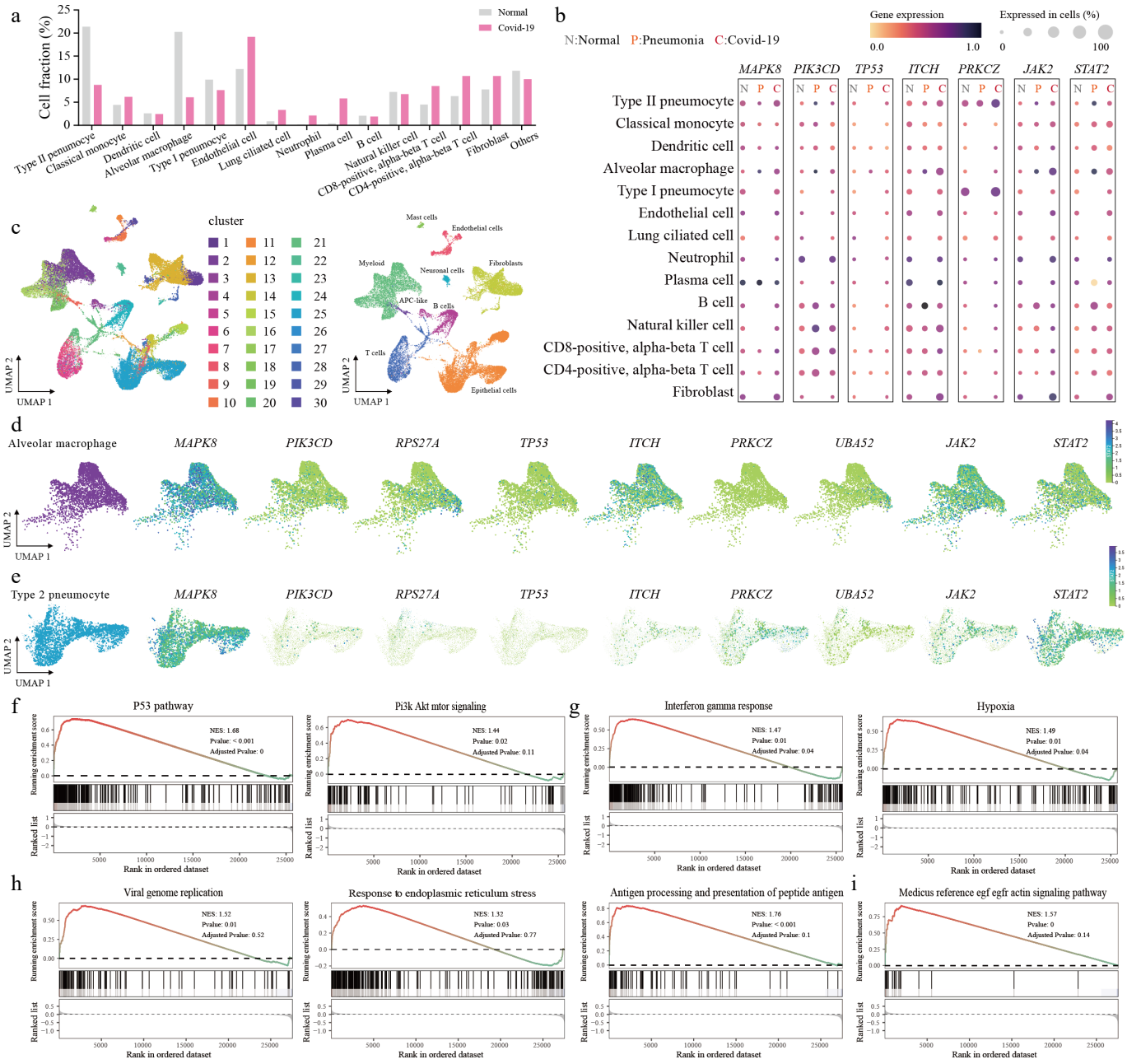


Fig. 4 Single-cell mapping unveils dual-compartment hub gene activation under severe pulmonary infectious stress. (a) Bar chart of relative cell fraction shifts across pulmonary cell populations between normal and severe infectious states. (b) Dot plot showing expression levels (color intensity) and detection frequencies (dot size) of seven regulatory hub genes across normal (N), pneumonia (P), and COVID-19 (C) conditions. (c) Global UMAP visualization displaying unbiased clustering (left) and annotated cell types (right). UMAP feature plots depicting the spatial distribution of all nine hub genes within (d) alveolar macrophages and (e) type II pneumocyte subpopulations. (f), (g) Hallmark GSEA for alveolar macrophages. (h), (i) GO biological process and KEGG pathway GSEA for type II pneumocytes.

alveolar epithelial cells, vKO mainly affected NF-κB signaling, IL-6-mediated inflammatory cascades, and triglyceride metabolism. Further analysis of the epithelial compartment identified changes in structural pathways, including cilium movement, syncytium formation by plasma membrane fusion, and actin filament organization (Supplementary Fig. S3). These changes may underlie the epithelial barrier dysfunction. The epithelial pathways were driven mainly by knockout of *RPS27A* and *PIK3CD*. *RPS27A* encodes a ubiquitin-ribosomal fusion protein[35], and its deletion collapses global translation. *PIK3CD* encodes the PI3K catalytic subunit p110δ[36]. These two genes act through structural and signaling functions. In mild alveolar macrophages, hub gene perturbation modulated T cell proliferation and viral response pathways. In severe neutrophils, the most affected processes included wound healing, antigen presentation, and syncytium formation.

Intervention heatmaps examined the Log_2FC trajectories of key intercellular communication mediators and lipid metabolism-associated genes after virtual knockout (Fig. 5g and h). Knockout of *JAK2*, *TP53*, and *PRKCZ* downregulated pathogenic ligands, receptors, and lipid-associated effectors, such as *TNF*, *IL1B*, *CXCL8*, and *SPP1*, in severe and mild alveolar macrophages and in severe neutrophils. In alveolar epithelial cells, vKO suppressed chemotactic

https://doi.org/10.48130/targetome-0026-0055

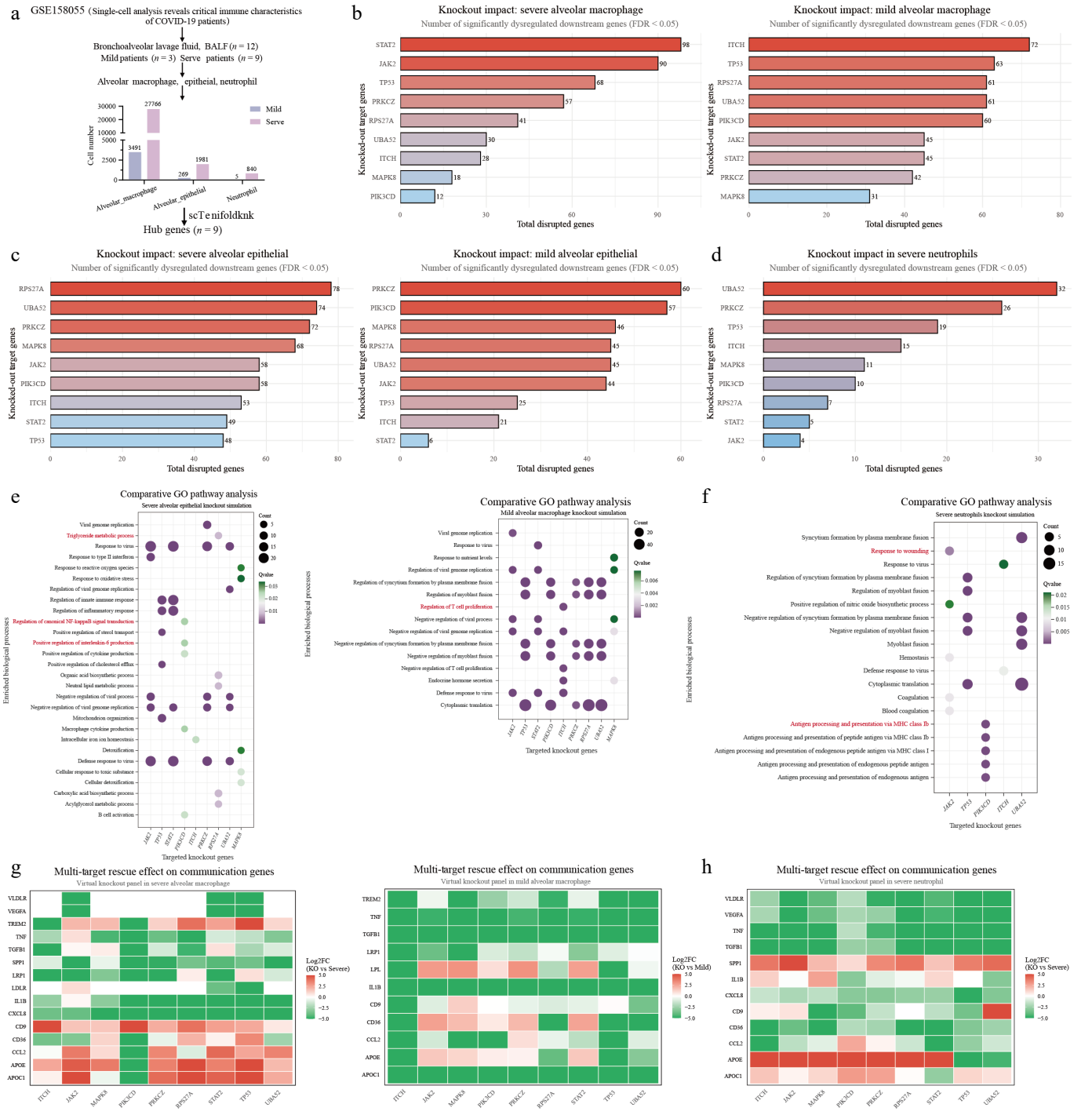


Fig. 5 *In silico* single-cell virtual knockout screening reveals the pathogenic essentiality and regulatory landscape of hub genes. (a) Schematic workflow of the virtual knockout (vKO) strategy. Bar plots quantifying global network disruption, defined as the number of significantly dysregulated downstream genes (FDR < 0.05), triggered by virtual deletion of individual hub genes across severe and mild (b) alveolar macrophages, (c) alveolar epithelial cells, and (d) severe neutrophils. (e), (f) Comparative gene ontology (GO) enrichment bubble plots detailing the functional landscape affected by vKO. Panel (e) displays distinct biological processes perturbed in severe alveolar epithelial cells (left) vs mild alveolar macrophages (right). (f) Illustrates the perturbed cascades in severe neutrophils. Intervention heatmaps display Log_2 Fold Change (Log_2FC) values of critical communication mediators and lipid-associated genes following targeted virtual knockout in (g) severe and mild alveolar macrophages and (h) severe neutrophils.

and lipid receptor genes, such as *CXCL8*, *CCL2*, and *LDLR* (Supplementary Fig. S3). These coordinated changes suggest that targeting these hub nodes may reverse the transcriptional alterations associated with infectious stress.

Network pharmacology screening and molecular docking identify curcumin and evodiamine as pleiotropic candidate dual-targeting agents against the immune-apoptotic triad

To translate the nine-gene hub signature into druggable targets, we performed network pharmacology screening using the HERB 2.0

database[23] to identify TCM bioactive ingredients capable of modulating the hub genes (Fig. 6a–d). An initial query returned 48 candidate compounds with documented target interactions. The distribution and overlap patterns of compound–target interactions were visualized *via* frequency bar charts, an UpSet plot, and a Sankey diagram mapping chemical classes to targets. Compounds were filtered by drug-likeness (DL ≥ 0.18), oral bioavailability (OB ≥ 30%), exclusion of primary metabolites and known toxins, and retention of compounds targeting ≥ 2 hub genes, yielding 33 TCM monomers classified into seven chemical groups, predominantly flavonoids and polyphenols.

A bipartite Cytoscape network analysis mapped interactions between the 33 retained compounds and the immune-apoptotic triad comprising *MAPK8*, *TP53*, and *JAK2* (Fig. 6e). Green nodes represented compounds targeting all three triad members; light purple nodes indicated dual-targeting agents. KEGG pathway enrichment analysis of the 33-compound library showed overlap with empyema-associated pathways identified in our earlier multi-omics profiling (Fig. 6f). Two independent evidence layers were integrated to prioritize candidates. First, a Comparative Toxicogenomics Database (CTD)-derived heatmap showed directional regulation of the triad genes by each candidate under normal and stress conditions (Fig. 6g). Second, *in silico* transcriptomic reversal analysis *via* the iLINCS L1000 database quantified each compound's capacity to reverse disease-associated transcriptional signatures from longitudinal patient profiles. Concordance scores were computed against week 1 vs week 3 and week 2 vs week 3 disease signatures (Fig. 6h). Among all candidates, curcumin and evodiamine emerged as the only dual-stage reversers.

TP53 was deprioritized from the druggable target list owing to its classification as a transcription factor with a shallow, featureless binding surface that lacks well-defined small-molecule binding pockets, as assessed by druggability score analysis.

Molecular docking simulations were conducted to evaluate binding interactions between curcumin/evodiamine and the catalytic domains of MAPK8 and JAK2. Three-dimensional binding surface visualizations and binding pocket orientations were generated for all four ligand-receptor pairs: curcumin-MAPK8 (Fig. 6i), evodiamine-MAPK8 (Fig. 6j), curcumin-JAK2 (Fig. 6k), and evodiamine-JAK2 (Fig. 6l). Two-dimensional interaction profiles identified non-covalent interactions, including hydrogen bonds, Pi-Pi stacking, and hydrophobic contacts, stabilizing ligand binding within each kinase domain (Supplementary Fig. S4a–S4d). These results support curcumin and evodiamine as candidate dual-targeting compounds for MAPK8 and JAK2.

Dynamic stability and thermodynamics of protein-ligand complexes *via* 100 ns molecular dynamics simulations

To characterize the binding stability and energetics of curcumin and evodiamine with MAPK8 and JAK2, we performed all-atom explicit-solvent molecular dynamics (MD) simulations over 100 ns followed by MM/PBSA binding free energy calculations. For the MAPK8-curcumin complex, root-mean-square deviation (RMSD) analysis showed that both protein backbone and ligand reached equilibrium within the first 20 ns and remained stable throughout the simulation (Fig. 7a). Per-residue free energy decomposition identified Lys55, Ile32, and neighboring residues as major contributors to binding affinity (Fig. 7b). Intermolecular hydrogen bond analysis showed two to five hydrogen bonds across most of the trajectory (Fig. 7c). Two-dimensional and three-dimensional Gibbs free energy landscape (FEL) projections along PC1 and PC2 converged on a single low-energy basin, indicating stable binding (Fig. 7d and e).

Parallel analysis was performed for the JAK2-evodiamine complex. RMSD profiles confirmed structural stability comparable to the MAPK8-curcumin system (Fig. 7f). Per-residue decomposition identified Leu892 and Glu896 as key residues contributing to evodiamine positioning within the catalytic domain (Fig. 7g). Hydrogen bond occupancy was lower than in the MAPK8-curcumin complex (Fig. 7h), consistent with a binding mode relying more on hydrophobic interactions. Both 2D and 3D FEL projections converged on a single dominant low-energy basin, indicating favorable complex formation (Fig. 7i and j).

Cross-combination simulations (curcumin-JAK2 and evodiamine-MAPK8) displayed moderate binding stability but weaker overall affinity and lower hydrogen bond occupancy compared with the preferred pairs (Supplementary Figs S5 and S6), supporting a preferential rather than exclusive targeting profile for each compound.

To assess protein structural integrity upon ligand binding, the radius of gyration (Rg) and solvent accessible surface area (SASA) were monitored across all four simulations (Supplementary Fig. S7a and S7b). Rg and SASA profiles remained stable with minimal fluctuations, indicating that neither curcumin nor evodiamine induced substantial protein unfolding or conformational changes upon binding.

MM/PBSA binding free energy calculations ranked curcumin-MAPK8 as the most favorable at −21.00 kcal·mol^{-1}, followed by evodiamine-JAK2 at −14.73 kcal·mol^{-1}[37] (Fig. 7k and l). Van der Waals interactions contributed > 60% of total binding energy in all complexes, with electrostatic contributions providing secondary stabilization. Per-residue decomposition identified hotspot residues critical for ligand recognition.

Pharmacological evaluation of MAPK8 and JAK2 inhibition in Kp-LPS-induced acute lung injury

In the natural product experiment, mice received intratracheal *K. pneumoniae*-derived LPS (Kp-LPS) as shown in Fig. 8a. The Model group showed progressive body weight loss and a significant reduction from baseline by day 3 ($P < 0.001$ vs Control) (Fig. 8b). Body weight decline was less pronounced in the Cur-H and Evo-H groups than in the Model group. The Combo group showed a weight trajectory similar to the high-dose monotherapy groups. Food intake declined sharply in all Kp-LPS-challenged groups on day 2. The Model group consumed about 40% of baseline, and the Combo group recovered most by day 3 (ns vs Control) (Fig. 8c).

H&E staining showed marked alveolar wall thickening and extensive inflammatory cell infiltration in the alveolar spaces of the Model group (Fig. 8d). Lung architecture was better preserved and inflammatory infiltration was substantially reduced in the Cur-H, Evo-H, and Combo groups. The lung dry-to-wet weight ratio reflects pulmonary water content, and lower values indicate more severe edema. This ratio was significantly lower in the Model group than in the Control group ($P < 0.001$), confirming that Kp-LPS induced marked pulmonary edema (Fig. 8e). The Cur-H, Evo-H, and Combo groups all showed significantly higher ratios than the Model group. BALF total protein, an indicator of alveolar-capillary barrier integrity, was significantly elevated in the Model group ($P < 0.001$ vs Control), and all natural product intervention groups reduced protein leakage (Fig. 8f).

In the inhibitor experiment, mice were treated as shown in Fig. 8g. The SP600125 (MAPK8i) and fedratinib (JAK2i) groups showed attenuated body weight loss relative to the Model group. The Dual-i group showed a weight trajectory similar to the

https://doi.org/10.48130/targetome-0026-0055

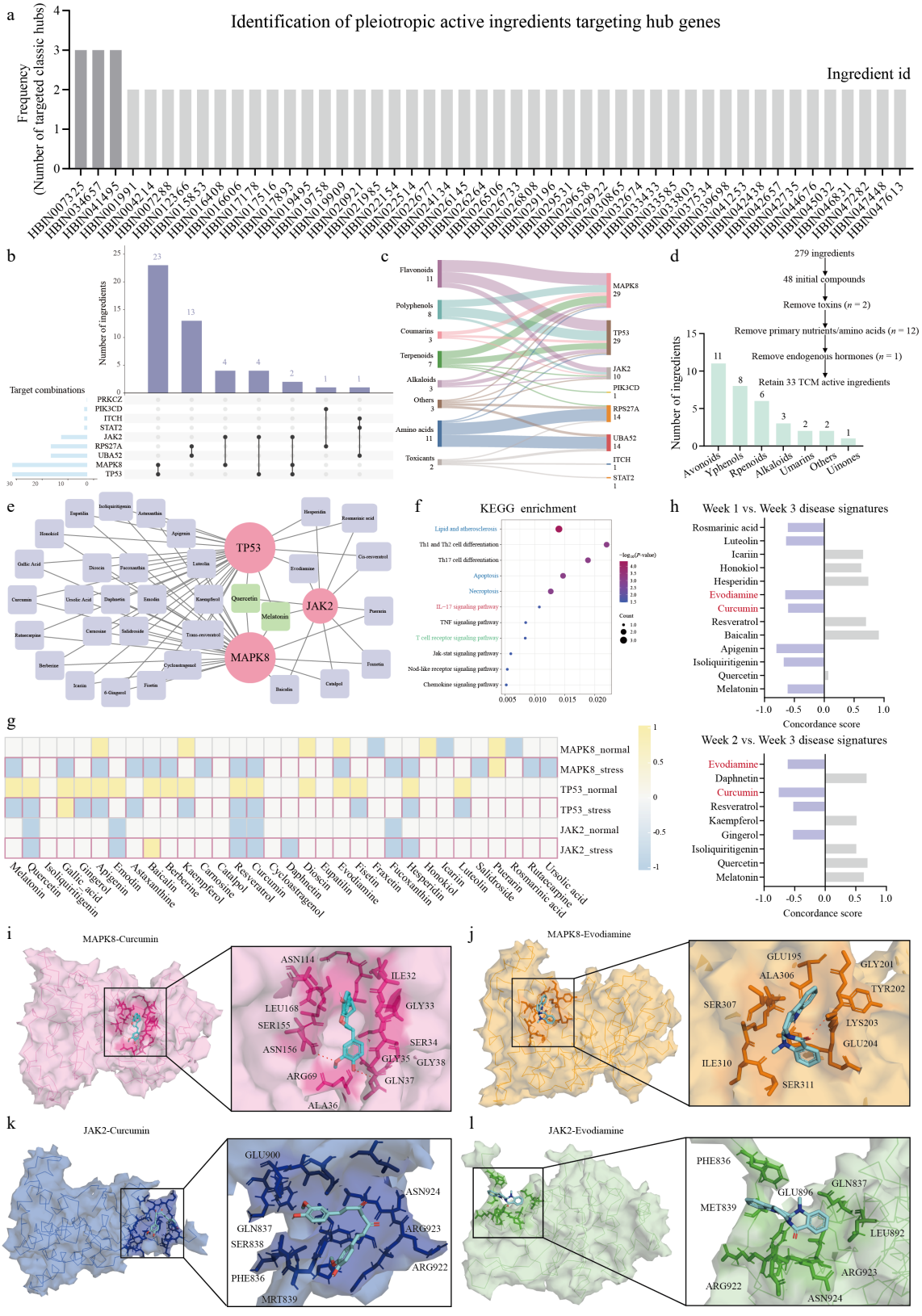
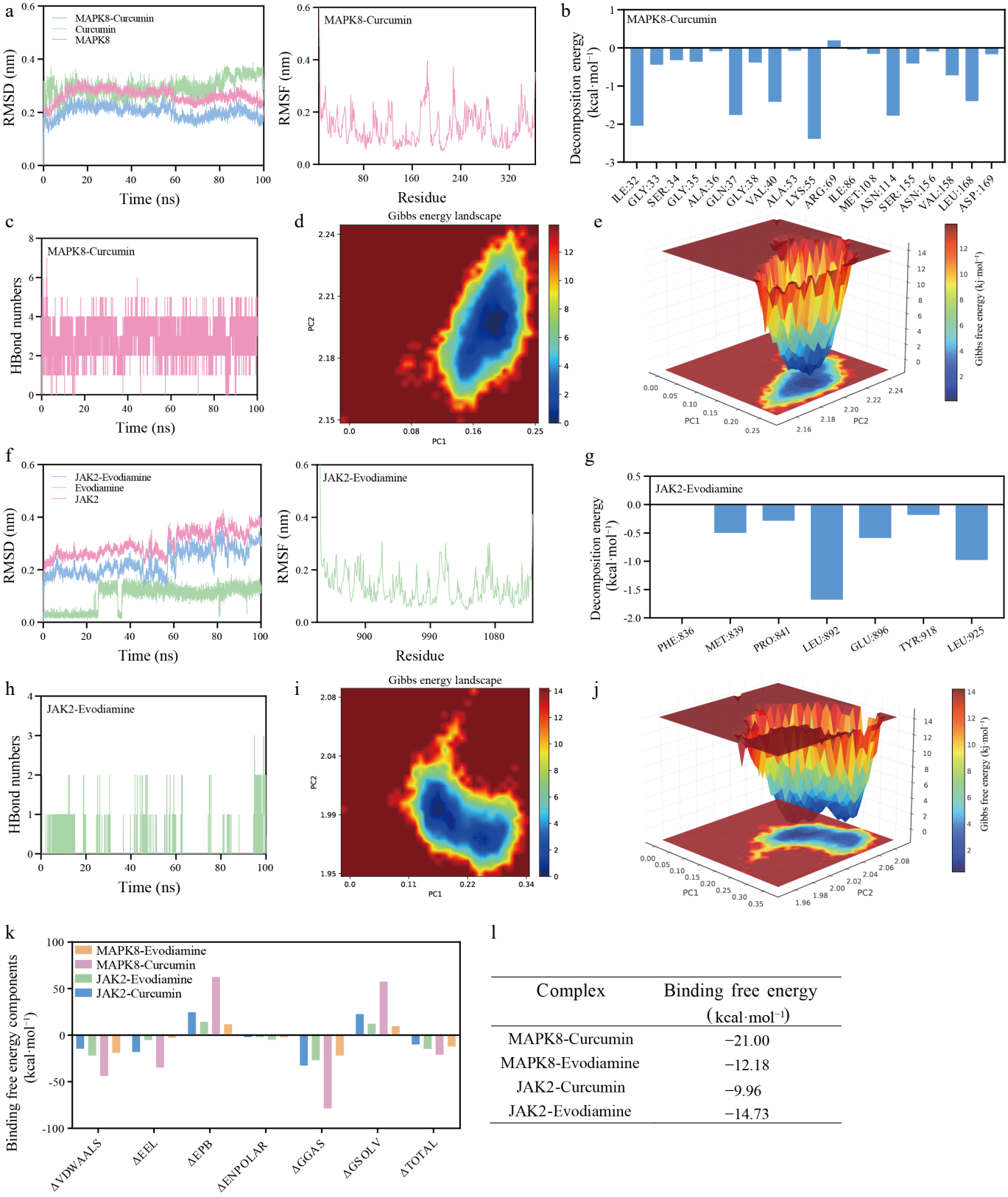


Fig. 6 Network pharmacology screening and molecular docking identify curcumin and evodiamine as candidate dual-targeting agents. (a) Frequency bar chart of TCM compounds from the HERB 2.0 database targeting host hub genes. (b) UpSet plot showing compound-target intersections. (c) Sankey diagram mapping chemical classes, ingredients, and targets. (d) Screening workflow and classification of 33 retained druggable TCM compounds into 7 chemical groups after removal of toxins and primary metabolites. (e) Bipartite Cytoscape network. (f) KEGG enrichment bubble plot of the 33 TCM compounds. (g) CTD-derived heatmap (−1: downregulation; +1: upregulation). (h) iLINCS L1000-based transcriptomic reversal analysis. Concordance Scores against Week 1 versus Week 3 (top) and Week 2 versus Week 3 (bottom) disease signatures. (i-l) Molecular docking simulations showing 3D binding surfaces and binding pocket orientations for the four ligand-receptor pairs: (i) curcumin-MAPK8, (j) evodiamine-MAPK8, (k) curcumin-JAK2, and (l) evodiamine-JAK2.



l

Complex	Binding free energy (kcal·mol^{-1})
MAPK8-Curcumin	−21.00
MAPK8-Evodiamine	−12.18
JAK2-Curcumin	−9.96
JAK2-Evodiamine	−14.73

Fig. 7 Dynamic stability and thermodynamics of protein-ligand complexes *via* 100 ns molecular dynamics simulations. Trajectory metrics and energy landscape for the MAPK8-curcumin complex: (a) root-mean-square deviation (RMSD) profiles of the protein backbone (pink), ligand (green), and complex (blue). (b) Per-residue decomposition energy plot showing amino acids contributing to binding free energy. (c) Time evolution of intermolecular hydrogen bond numbers. (d) Two-dimensional Gibbs free energy landscape (FEL) along PC1 and PC2. (e) Three-dimensional FEL. Parallel MD trajectory analysis for the JAK2-evodiamine complex: (f) RMSD profile. (g) per-residue decomposition energy showing key binding residues. (h) Hydrogen bond trajectory. (i) 2D FEL. (j) 3D FEL. (k) MM/PBSA binding free energy components (van der Waals, electrostatic, polar solvation, non-polar solvation) for all four compound-target combinations. (l) Summary table of calculated total binding free energies (kcal·mol^{-1}).

https://doi.org/10.48130/targetome-0026-0055

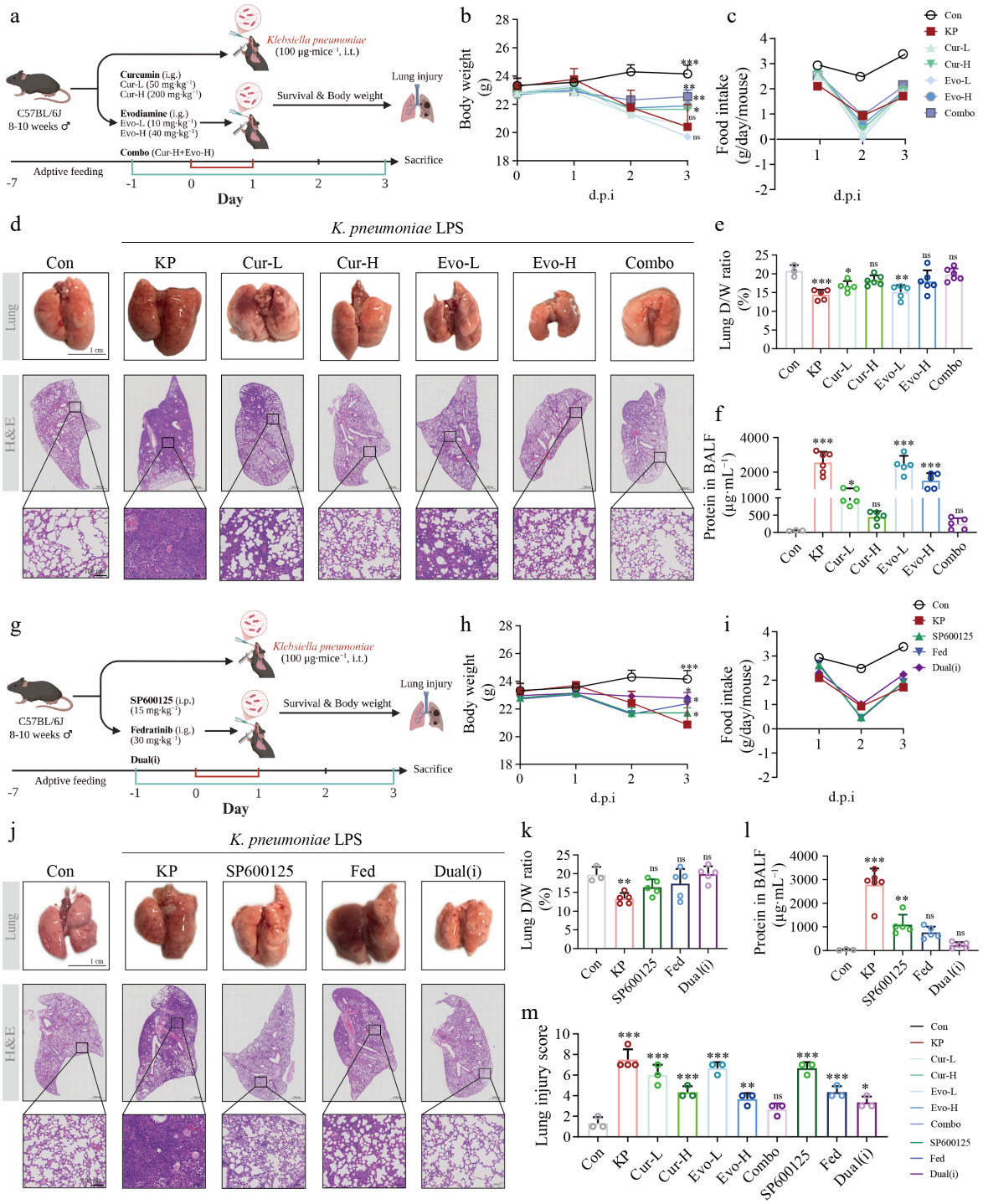


Fig. 8 Pharmacological evaluation of curcumin, evodiamine, and selective inhibitors in *K. pneumoniae* LPS-induced acute lung injury in mice. (a) Schematic of the natural product experimental protocol. (b) Body weight change curves for natural product treatment groups (mean ± SEM). (c) Food intake for natural product treatment groups (g/cage/d). (d) Representative H&E-stained lung sections from natural product treatment groups (scale bar = 100 μm). (e) Lung dry-to-wet weight ratio (%) for natural product treatment groups. (f) Total protein concentration in bronchoalveolar lavage fluid (BALF) from natural product treatment groups. (g) Schematic of the inhibitor experimental protocol. (h) Body weight change curves for inhibitor treatment groups (mean ± SEM). (i) Food intake for inhibitor treatment groups (g/cage/d). (j) Representative H&E-stained lung sections from inhibitor treatment groups (scale bar = 100 μm). (k) Lung dry-to-wet weight ratio (%) for inhibitor treatment groups. (l) BALF total protein concentration for inhibitor treatment groups. (m) Lung injury score (0–10 scale, blinded assessment). C57BL/6J mice were randomly assigned to groups. The natural product experiment comprised seven groups: vehicle control (Control, $n = 4$), Kp-LPS challenge (Model, $n = 12$), low-dose curcumin (Cur-L, 50 mg·kg^{-1}, $n = 5$), high-dose curcumin (Cur-H, 200 mg·kg^{-1}, $n = 6$), low-dose evodiamine (Evo-L, 10 mg·kg^{-1}, $n = 5$), high-dose evodiamine (Evo-H, 40 mg·kg^{-1}, $n = 6$), and combination therapy (Combo, Cur-H + Evo-H, $n = 10$). The inhibitor experiment comprised five groups: Control, Model, the MAPK8 inhibitor SP600125 (15 mg·kg^{-1}, i.p., $n = 5$), the JAK2 inhibitor fedratinib (30 mg·kg^{-1}, i.g., $n = 5$), and dual inhibitor combination (Dual-i, $n = 5$). Drugs were administered once daily *via* oral gavage; *Klebsiella pneumoniae*-derived LPS (100 μg/mouse) was delivered by intratracheal instillation. Mice were sacrificed at the day 3 endpoint. Data are presented as mean ± SEM. * $P < 0.05$, ** $P < 0.01$, *** $P < 0.001$ vs Control; ns, not significant. Body weight and food intake were analyzed by two-way repeated-measures ANOVA; all other parameters were analyzed by one-way ANOVA followed by Tukey's post hoc test.

individual inhibitor groups (Fig. 8h). Food intake paralleled the natural product experiment, with a nadir on day 2 and partial recovery thereafter in all inhibitor-treated groups (Fig. 8i). Both SP600125 and fedratinib attenuated lung tissue injury relative to the Model group. The Dual-i group showed the most pronounced improvement (Fig. 8j). For the dry-to-wet weight ratio, the Dual-i group showed the greatest recovery among the inhibitor-treated groups (Fig. 8k). For BALF total protein, the fedratinib and Dual-i groups showed the most pronounced reductions among the inhibitor-treated groups (Fig. 8l).

Blinded lung injury scoring of H&E sections (0–10 scale) provided quantitative confirmation. The Model group received the highest scores among all groups ($P < 0.001$ vs Control). The Cur-H and Evo-H groups scored significantly lower than the Model group, and the Combo group showed a further reduction (Fig. 8m). Within the inhibitor arm, the Dual-i group had the lowest score, with the SP600125 and fedratinib groups falling between the Model and Dual-i groups. Together, these results show that curcumin, evodiamine, and the selective inhibitors of MAPK8 and JAK2 each attenuate Kp-LPS-induced body weight loss, pulmonary edema, alveolar-capillary barrier disruption, and lung histopathological injury to varying degrees.

Target engagement and anti-inflammatory mechanisms of curcumin and evodiamine in Kp-LPS-induced ALI

To validate direct target engagement at the endogenous protein level, we performed an in-cell CETSA in A549 cells. Both kinases were immunoblotted across all treatment groups in a cross-target design. Curcumin (40 μmol·L^{-1}) markedly shifted the apparent melting temperature of MAPK8 from 51.05 °C (DMSO) to 57.80 °C (ΔT_m = +6.8 °C), but did not stabilize JAK2 (ΔT_m = +0.2 °C). This indicates preferential intracellular binding of curcumin to MAPK8. Evodiamine (40 μmol·L^{-1}) modestly stabilized both MAPK8 and JAK2 (ΔT_m = +2.3 °C each), consistent with the dual engagement predicted by our molecular dynamics simulations (Fig. 9a and b). These results provide direct biochemical evidence that curcumin and evodiamine engage MAPK8 and JAK2 within intact cells.

Having confirmed intracellular target engagement, we next examined the signaling consequences. We measured the phosphorylation of the JAK/STAT[38] and JNK/MAPK pathways in lung tissues at 72 h after Kp-LPS challenge by western blot. The *p*-JAK2/JAK2 and *p*-JNK/MAPK8 ratios were significantly higher in the Model group than in the Control group ($P = 0.02$ and $P = 0.04$, respectively). This indicates that Kp-LPS activated JAK2 and MAPK8 phosphorylation in lung tissues (Fig. 9c and d). After pharmacological intervention, only the Combo group significantly reduced both ratios relative to the Model group and restored both pathways to levels not significantly different from Control. The Cur-H and Evo-H groups each attenuated one pathway without significantly suppressing both, consistent with the target preference of each compound. Combined treatment therefore effectively suppressed Kp-LPS-induced activation of both the JAK2 and MAPK8 pathways *in vivo*.

To further dissect the roles of MAPK8 and JAK2 in Kp-LPS-induced pulmonary inflammatory signaling, we used the selective inhibitors SP600125 and fedratinib to block each pathway independently. SP600125 significantly reduced the *p*-JNK/MAPK8 ratio relative to the Model group ($P = 0.003$) and also reduced the *p*-JAK2/JAK2 ratio. This suggests that MAPK8 inhibition may indirectly suppress JAK2 phosphorylation through inter-pathway crosstalk. Fedratinib partially reduced the *p*-JNK/MAPK8 ratio, but the *p*-JAK2/JAK2 ratio remained elevated relative to the Control. This indicates that JAK2 inhibition alone had limited efficacy at the 72-h time point. In the Dual-i group, both the *p*-JAK2/JAK2 and *p*-JNK/MAPK8 ratios were significantly reduced relative to the Model group (both $P < 0.001$) and were restored to levels not significantly different from Control, indicating suppression of both pathways to baseline levels (Fig. 9e and f).

Immunofluorescence dual staining revealed substantial infiltration of F4/80$^+$ macrophages (green) and Ly6G$^+$ neutrophils (red) in the lung tissues of the Model group compared with the Control. Both cell types were distributed within alveolar spaces and the pulmonary interstitium (Fig. 9g). The numbers of both F4/80$^+$ and Ly6G$^+$ cells were markedly reduced in the Cur-H, Evo-H, and Combo groups. The Combo group showed fluorescence intensities for both populations that most closely matched those of the Control group.

Masson's trichrome staining was used to evaluate collagen deposition in lung tissue. Quantitative analysis showed minimal differences in collagen area percentage across groups (ns vs Control). No significant fibrotic remodeling had occurred by 72 h after Kp-LPS challenge, consistent with the pathological time course of acute lung injury (Fig. 9h and i).

Serum levels of pro-inflammatory and pro-fibrotic cytokines were measured by ELISA. IL-1β, TNF-α, and TGF-β1 levels in the Model group were significantly higher than in the Control group ($P < 0.001$). This indicates that intratracheal Kp-LPS instillation elicited both local pulmonary inflammation and a systemic inflammatory response (Fig. 9j–l). All three cytokines were significantly reduced in the Cur-H and Evo-H groups. The Combo group achieved the most pronounced suppression of IL-1β and TNF-α, with levels restored to values not significantly different from Control (ns vs Control). Collectively, these results show that curcumin and evodiamine attenuate Kp-LPS-induced local pulmonary inflammation and suppress systemic inflammatory cytokine release.

Discussion

The therapeutic management of severe *K. pneumoniae* empyema is limited by a lack of pharmacological agents that address both pathogen survival mechanisms and host immune-metabolic dysregulation[39]. Furthermore, the index patient had concurrent HBV infection (Supplementary Table S1), which may introduce immunologic confounding that warrants consideration when interpreting the host transcriptional signatures. While conventional approaches focus primarily on antimicrobial eradication, our multi-omics integration suggests that effective intervention may require concurrent targeting of pathogen metabolic pathways and host transcriptional regulators[40–42]. Future studies should enroll multicenter cohorts of hvKp empyema patients with systematic clinical metadata to validate and extend these findings.

A key finding from metabolomic profiling is taurine-associated host–pathogen co-metabolism. Taurine is enriched in host leukocytes for oxidative stress response and mucosal immunity modulation[43]. Our longitudinal data showed progressive taurine depletion with disease progression, indicating that pathogen-mediated taurine utilization may represent a virulence mechanism that reduces host antioxidant capacity while supporting microbial sulfur assimilation[44].

On the host side, integrated transcriptomic profiling identified three central genes (*MAPK8*, *JAK2*, and *TP53*) that form an interconnected signaling module. Single-cell spatial mapping showed elevated expression of this signaling axis in alveolar macrophages engaged in lipid clearance, while concurrent stress signaling in type II pneumocytes was associated with apoptosis.

https://doi.org/10.48130/targetome-0026-0055

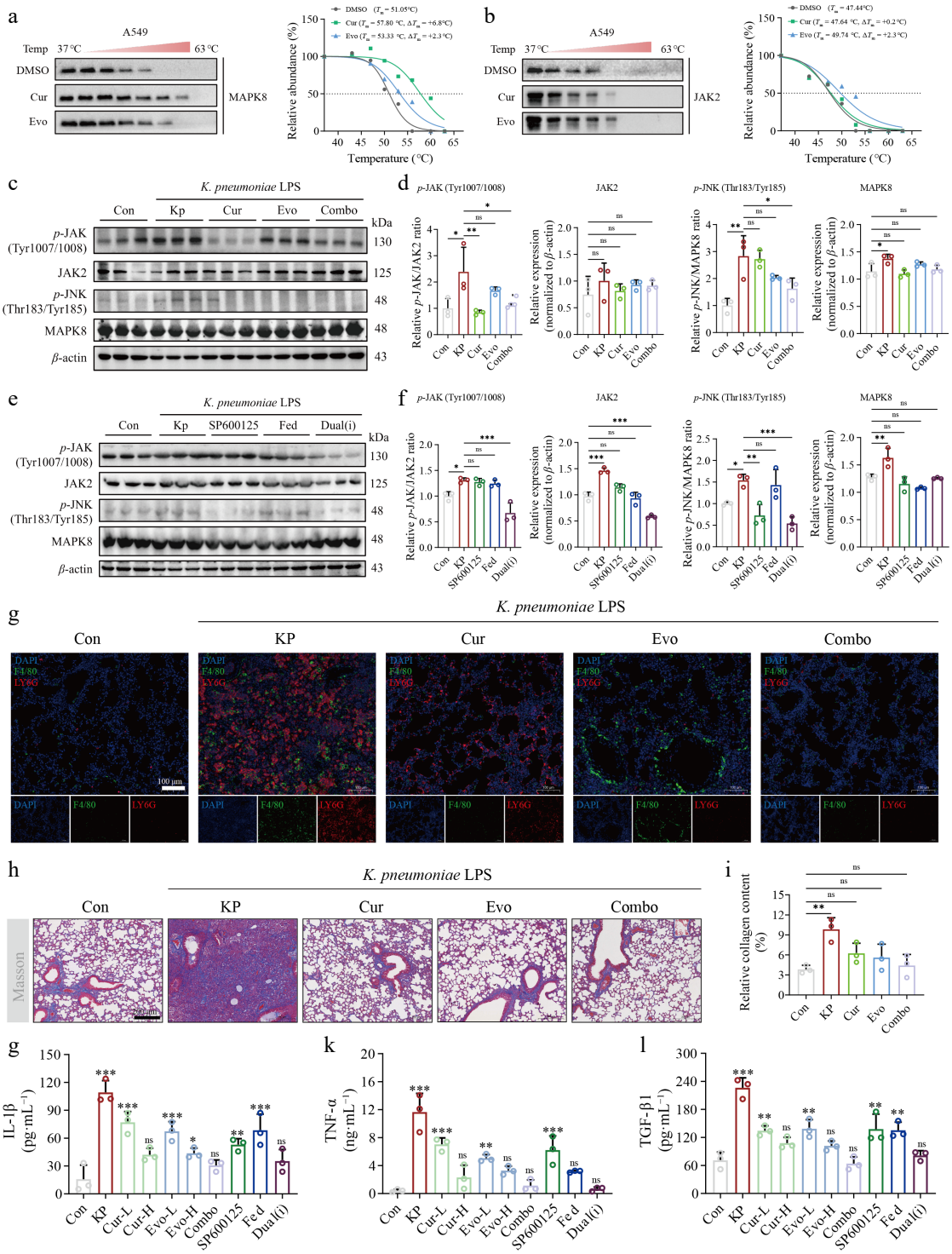


Fig. 9 Target engagement and *in vivo* signaling pathway modulation of curcumin and evodiamine in *K. pneumoniae* LPS-induced ALI. (a) CETSA of MAPK8 in A549 cells treated with DMSO, curcumin (40 μmol·L^{-1}), or evodiamine (40 μmol·L^{-1}); (b) CETSA of JAK2 under the same conditions. Soluble protein was normalized to the 37 °C value and fitted to a four-parameter logistic model; the dotted line indicates 50% soluble protein. (c) Representative western blot images of *p*-JAK (Tyr1007/1008), JAK2, *p*-JNK (Thr183/Tyr185), and MAPK8 in lung tissues from natural product-treated groups, with *β*-actin as the loading control. (d) Densitometric quantification of (c). Phospho-to-total protein ratios (*p*-JAK/JAK2 and *p*-JNK/MAPK8) were normalized to the Control group, with drug-treated groups compared against the Model group; total JAK2 and MAPK8 expression was normalized to *β*-actin and expressed relative to the Control group. (e) Representative western blot images of *p*-JAK (Tyr1007/1008), JAK2, *p*-JNK (Thr183/Tyr185), and MAPK8 in lung tissues from inhibitor-treated groups, with *β*-actin as the loading control. (f) Densitometric quantification of (e). Phospho-to-total protein ratios (*p*-JAK/JAK2 and *p*-JNK/MAPK8) were normalized to the Control group, with inhibitor-treated groups compared against the Model group; total JAK2 and MAPK8 expression was normalized to *β*-actin and expressed relative to the Control group. (g) Representative immunofluorescence images of F4/80 (green, macrophages) and Ly6G (red, neutrophils) dual staining in lung tissue (scale bar = 100 μm), with DAPI (blue) counterstaining nuclei. (h) Quantification of collagen area (%) by Masson's trichrome staining. (i) Representative Masson's trichrome-stained sections for each group (scale bar = 200 μm). (j)–(l) Serum levels of IL-1β, TNF-α, and TGF-β1 measured by ELISA. Data are presented as mean ± SEM. * $P < 0.05$, ** $P < 0.01$, *** $P < 0.001$ vs Control; ns, not significant. One-way ANOVA followed by Tukey's post hoc test.

We applied the machine learning algorithm scTenifoldKnk for *in silico* virtual knockout screening. This approach models the systems-level consequences of targeted gene perturbation, providing a computational framework to infer functional relationships between individual hub genes and the infectious transcriptional program. Similar integrated computational-experimental validation strategies have been applied in network pharmacology studies of natural products[45].

To identify candidate compounds targeting these genes, we used network pharmacology and the iLINCS transcriptomic perturbation database. While TP53 has limited drug accessibility due to its structural properties, we note that MAPK8 and JAK2 inhibition may exert downstream effects on p53-mediated apoptotic and stress-response pathways, potentially offering indirect modulation of the triad. The kinases MAPK8 and JAK2 are more tractable targets. Docking and molecular dynamics simulations predicted that curcumin binds stably to MAPK8 and evodiamine to JAK2, consistent with reported anti-inflammatory activities of these natural products.

However, curcumin has two recognized limitations. It is a pan-assay interference compound (PAINS) that can generate false-positive hits in cell-free assays, and it has very low oral bioavailability because of poor aqueous solubility, rapid first-pass metabolism, and chemical instability at physiological pH. These liabilities limit its translational value despite the favorable computational and *in vivo* results reported here. The PAINS concern applies mainly to cell-free screening assays, in which curcumin can give false-positive hits through assay interference. Our target-binding evidence does not rely on such assays. It is instead based on a cellular thermal shift assay that measures binding within intact cells, together with *in vivo* efficacy data. These orthogonal approaches are not subject to the false-positive risk that the PAINS designation warns against. Several strategies can address these limitations. Structural modification of the β-diketone and diene moieties yields more stable and more bioavailable derivatives such as tetrahydrocurcumin and hexahydrocurcumin[46]. Delivery systems including cyclodextrin complexes, liposomes, and polymeric nanocarriers improve solubility and prolong circulation. For a pulmonary target, inhalation or intratracheal delivery deposits the drug directly in the inflamed lung and lowers the required dose. Cyclodextrin-complexed curcumin delivered to the lung reduced injury and mortality in *K. pneumoniae* pneumonia, and inhaled liposomal curcumin attenuated acute lung injury[47,48]. Evodiamine has hepatotoxic potential that is linked to CYP3A4-mediated metabolic activation[49]. Blocking this activation site by structural modification is a rational route to safer derivatives, and evodiamine derivatives with reduced cytotoxicity and delivery systems that improve its solubility have been reported[50]. These combined strategies support further development of both compounds toward clinical translation.

In vivo pharmacological evaluation using a *K. pneumoniae* LPS-induced murine ALI model provided the first experimental evidence supporting the therapeutic potential of MAPK8/JAK2 dual inhibition. Curcumin and evodiamine, both alone and in combination, significantly attenuated pulmonary edema, alveolar-capillary barrier disruption, and histopathological lung injury. Combination therapy showed a trend toward superior efficacy in reducing inflammatory cytokine release. Although *in vitro* synergy between curcumin and evodiamine has been reported[51], formal synergy analysis was not conducted here, precluding definitive conclusions about additive or synergistic effects *in vivo*. Western blot analysis confirmed that curcumin preferentially reduced the *p*-JNK/MAPK8 ratio while evodiamine predominantly reduced the *p*-JAK2/JAK2 ratio in lung tissues. Furthermore, CETSA provided direct evidence of intracellular target engagement, showing that curcumin preferentially stabilizes MAPK8 without stabilizing JAK2, collectively validating the computational binding predictions at both the target-engagement and signaling levels. MAPK8 inhibition by SP600125 also led to reduced JAK2 phosphorylation, suggesting inter-pathway crosstalk that may contribute to the broader anti-inflammatory effects of MAPK8-targeted intervention. The reduction in F4/80$^+$ macrophage and Ly6G$^+$ neutrophil infiltration in treated groups is consistent with the single-cell transcriptomic evidence that these cell types are the primary compartments of hub gene activation. These *in vivo* findings establish a functional bridge between the computational predictions and translational relevance of dual MAPK8/JAK2 targeting.

This study has several limitations. First, the longitudinal multi-omics data were derived from a single patient. Although findings were compared with external transcriptomic and single-cell datasets (e.g., GSE76293, GSE171524), prospective multi-center cohorts would further support generalizability. Of note, the external transcriptomic cohorts consisted of ARDS and COVID-19 patients rather than confirmed hvKp empyema cases. While the shared inflammatory pathology across these conditions supports the pan-disease relevance of the hub gene signature, the distinct etiologies warrant cautious interpretation. Second, the *K. pneumoniae* LPS-induced murine model, while reproducing key inflammatory features of Gram-negative pneumonia, cannot recapitulate live bacterial proliferation, virulence factor secretion, or the polymicrobial milieu of clinical empyema. Consequently, the K15373 metabolic vulnerability hypothesis could not be tested in this model and will require live *K. pneumoniae* infection studies for validation. Third, *in silico* predictions, including virtual perturbations and molecular dynamics simulations, require experimental validation through assays such as macrophage-pathogen co-culture and pharmacokinetic profiling. Fourth, target engagement was assessed by CETSA. This assay reports binding-induced thermal stabilization, but it does not yield IC_{50} or K_d values. The binding affinity of curcumin and evodiamine for MAPK8 and JAK2 therefore remains unmeasured. Surface plasmon resonance, isothermal titration calorimetry, and *in vitro* kinase activity assays will be required to obtain these values and to confirm whether the therapeutic effects arise from direct dual-target inhibition or from single-target inhibition with downstream crosstalk.

Conclusions

In summary, this study characterized metabolic and transcriptomic features of the *K. pneumoniae* empyema microenvironment through integrated multi-omics analysis. Single-cell virtual knockout and molecular dynamics simulations indicated that MAPK8, JAK2, and the computationally predicted bacterial vulnerability K15373 contribute to macrophage-associated inflammation, epithelial barrier disruption, and pathogen survival, representing candidate therapeutic targets. Curcumin and evodiamine were predicted to bind stably to MAPK8 and JAK2, respectively, and counteracted the disease-associated transcriptional signature in perturbation assays. *In vivo* pharmacological experiments using a *K. pneumoniae* LPS-induced ALI model confirmed that curcumin and evodiamine attenuated pulmonary inflammation and edema, with CETSA, western blot, and immunofluorescence analyses validating target engagement and downstream pathway modulation at the cellular, signaling, and tissue levels. This integrated computational-experimental framework provides a basis for further development of host-directed therapies against severe *K. pneumoniae* empyema (Supplementary Fig. S8).

Ethical statements

Human Subjects: This study was conducted in accordance with the Declaration of Helsinki and approved by the Ethics Committee of the Affiliated Hospital of Nanjing University of Chinese Medicine (Approval No. 2025NL-025-02; February 8, 2025). Written informed consent was obtained from the patient prior to sample collection. Animal model: Male C57BL/6 mice (8 weeks old) were purchased from Gempharmatech. All animal experiments were conducted in accordance with the NIH Guide for the Care and Use of Laboratory Animals and approved by the Institutional Animal Care and Use Committee of Nanjing University (IACUC2410004). During the preparation of this work, the authors used R language and Python-based tools for data processing and figure generation. The authors reviewed and edited all content produced with the assistance of these tools, verified its accuracy, and take full responsibility for the integrity and originality of the final manuscript. This work represents the authors' own intellectual contribution, and no AI tool is credited as an author.

Author contributions

The authors confirm their contribution to the paper as follows: study conception and design: Wu X, Zhang Y, Lin Y; data collection: Zhang Y, Luo K, Zhang J, Li Y; analysis and interpretation of results: Zhang Y, Lin Y, Luo K, Zhang J, Li Y, Lu X; draft manuscript preparation: Zhang Y, Yi H, Wu X. manuscript revision: Zhang Y, Wu X; funding acquisition: Wu X, Lu X, Yi H, Du R. The primary corresponding author: Wu X. All authors reviewed the results and approved the final version of the manuscript.

Data availability

The datasets generated and analyzed during the current study have been deposited in established public repositories. The untargeted metabolomics data have been deposited in the EMBL-EBI MetaboLights database under the accession number MTBLS14738. The raw bulk RNA sequencing data have been deposited in the NCBI Sequence Read Archive (SRA) under the BioProject accession number PRJNA1476439. Both datasets are currently under embargo and will be made publicly available upon the publication of this manuscript. In the interim, access to the data for peer-review purposes or reasonable academic requests can be obtained by contacting the corresponding authors. The public single-cell RNA sequencing datasets analyzed in this study (GSE171524, GSE158055, and GSE76293) are openly available in the Gene Expression Omnibus (GEO) repository.

Acknowledgments

This work was supported by the National Natural Science Foundation of China (Grant Nos 82373931 and 82675099 to Wu X, 81774081 to Lu X, 82373882 to Yi H, and 82373884 to Du R), the Basic Research Program of Jiangsu (Grant No. BK20251992), and the Lingang Laboratory (Grant No. LGL-2612-12) to Wu X.

Conflict of interest

The authors have no conflict of interest to declare.

Supplementary information accompanies this paper online at: https://doi.org/10.48130/targetome-0026-0055.

Dates

Received 14 June 2026; Revised 29 September 2026; Accepted 8 October 2026; Published online 5 November 2026

References

[1] Gu D, Dong N, Zheng Z, Lin D, Huang M, et al. 2018. A fatal outbreak of ST11 carbapenem-resistant hypervirulent *Klebsiella pneumoniae* in a Chinese hospital: a molecular epidemiological study. *The Lancet Infectious Diseases* 18:37–46

[2] Hu F, Pan Y, Li H, Han R, Liu X, et al. 2024. Carbapenem-resistant *Klebsiella pneumoniae* capsular types, antibiotic resistance and virulence factors in China: a longitudinal, multi-centre study. *Nature Microbiology* 9:814–829

[3] Xu Q, Xie M, Liu X, Heng H, Wang H, et al. 2023. Molecular mechanisms underlying the high mortality of hypervirulent *Klebsiella pneumoniae* and its effective therapy development. *Signal Transduction and Targeted Therapy* 8:221

[4] Murray CJL, Ikuta KS, Sharara F, Swetschinski L, Robles Aguilar G, et al. 2022. Global burden of bacterial antimicrobial resistance in 2019: a systematic analysis. *The Lancet* 399:629–655

[5] Yang X, Sun Q, Li J, Jiang Y, Li Y, et al. 2022. Molecular epidemiology of carbapenem-resistant hypervirulent *Klebsiella pneumoniae* in China. *Emerging Microbes & Infections* 11:841–849

[6] Pu D, Zhao J, Chang K, Zhuo X, Cao B. 2023. 'Superbugs' with hypervirulence and carbapenem resistance in *Klebsiella pneumoniae*: the rise of such emerging nosocomial pathogens in China. *Science Bulletin* 68:2658–2670

[7] Rahman NM, Maskell NA, West A, Teoh R, Arnold A, et al. 2011. Intrapleural use of tissue plasminogen activator and DNase in pleural infection. *New England Journal of Medicine* 365:518–526

[8] Wyres KL, Lam MMC, Holt KE. 2020. Population genomics of *Klebsiella pneumoniae*. *Nature Reviews Microbiology* 18:344–359

[9] Zumla A, Rao M, Wallis RS, Kaufmann SHE, Rustomjee R, et al. 2016. Host-directed therapies for infectious diseases: current status, recent progress, and future prospects. *The Lancet Infectious Diseases* 16:e47–e63

[10] Kaufmann SHE, Dorhoi A, Hotchkiss RS, Bartenschlager R. 2018. Host-directed therapies for bacterial and viral infections. *Nature Reviews Drug Discovery* 17:35–56

[11] Ferreiro L, Toubes ME, Suárez-Antelo J, Rodríguez-Núñez N, Valdés L. 2024. Clinical overview of the physiology and pathophysiology of pleural fluid movement: a narrative review. *ERJ Open Research* 10:00050-2024

[12] Wong Fok Lung T, Charytonowicz D, Beaumont KG, Shah SS, Sridhar SH, et al. 2022. *Klebsiella pneumoniae* induces host metabolic stress that promotes tolerance to pulmonary infection. *Cell Metabolism* 34:761–774.e769

[13] Hsueh PC, Wu KA, Yang CY, Hsu CW, Wang CL, et al. 2020. Metabolomic profiling of parapneumonic effusion reveals a regulatory role of dipeptides in interleukin-8 production in neutrophil-like cells. *Analytica Chimica Acta* 1128:238–250

[14] Dumigan A, Cappa O, Morris B, Sá Pessoa J, Calderon-Gonzalez R, et al. 2022. *In vivo* single-cell transcriptomics reveal *Klebsiella pneumoniae* skews lung macrophages to promote infection. *EMBO Molecular Medicine* 14:e16888

[15] Zhai Y, Liu L, Zhang F, Chen X, Wang H, et al. 2025. Network pharmacology: a crucial approach in traditional Chinese medicine research. *Chinese Medicine* 20:8

[16] Li S, Zhang B. 2013. Traditional Chinese medicine network pharmacology: theory, methodology and application. *Chinese Journal of Natural Medicines* 11:110–120

[17] Nogales C, Mamdouh ZM, List M, Kiel C, Casas AI, et al. 2022. Network pharmacology: curing causal mechanisms instead of treating symptoms. *Trends in Pharmacological Sciences* 43:136–150

[18] Wang Y, Wang Y, Cai N, Xu T, He F. 2021. Anti-inflammatory effects of curcumin in acute lung injury: *in vivo* and *in vitro* experimental model studies. *International Immunopharmacology* 96:107600

[19] Russo TA, Marr CM. 2019. Hypervirulent *Klebsiella pneumoniae*. *Clinical Microbiology Reviews* 32:e00001-19
[20] Pang Z, Chong J, Zhou G, de Lima Morais DA, Chang L, et al. 2021. MetaboAnalyst 5.0: narrowing the gap between raw spectra and functional insights. *Nucleic Acids Research* 49:W388–W396
[21] Osorio D, Zhong Y, Li G, Xu Q, Yang Y, et al. 2022. scTenifoldKnk: an efficient virtual knockout tool for gene function predictions *via* single-cell gene regulatory network perturbation. *Patterns* 3:100434
[22] Yang Y, Li G, Zhong Y, Xu Q, Chen BJ, et al. 2023. Gene knockout inference with variational graph autoencoder learning single-cell gene regulatory networks. *Nucleic Acids Research* 51:6578–6592
[23] Gao K, Liu L, Lei S, Li Z, Huo P, et al. 2025. HERB 2.0: an updated database integrating clinical and experimental evidence for traditional Chinese medicine. *Nucleic Acids Research* 53:D1404–D1414
[24] Shannon P, Markiel A, Ozier O, Baliga NS, Wang JT, et al. 2003. Cytoscape: a software environment for integrated models of biomolecular interaction networks. *Genome Research* 13:2498–2504
[25] Liu Y, Yang X, Gan J, Chen S, Xiao ZX, et al. 2022. CB-Dock2: improved protein-ligand blind docking by integrating cavity detection, docking and homologous template fitting. *Nucleic Acids Research* 50:W159–W164
[26] Vanommeslaeghe K, Hatcher E, Acharya C, Kundu S, Zhong S, et al. 2010. CHARMM general force field: a force field for drug-like molecules compatible with the CHARMM all-atom additive biological force fields. *Journal of Computational Chemistry* 31:671–690
[27] Best RB, Zhu X, Shim J, Lopes PEM, Mittal J, et al. 2012. Optimization of the additive CHARMM all-atom protein force field targeting improved sampling of the backbone ϕ, ψ and side-chain χ_1 and χ_2 dihedral angles. *Journal of Chemical Theory and Computation* 8:3257–3273
[28] Bennett BL, Sasaki DT, Murray BW, O'Leary EC, Sakata ST, et al. 2001. SP600125, an anthrapyrazolone inhibitor of Jun N-terminal kinase. *Proceedings of the National Academy of Sciences of the United States of America* 98:13681–13686
[29] Wernig G, Kharas MG, Okabe R, Moore SA, Leeman DS, et al. 2008. Efficacy of TG101348, a selective JAK2 inhibitor, in treatment of a murine model of JAK_2V617F-induced polycythemia vera. *Cancer Cell* 13:311–320
[30] Martinez Molina D, Jafari R, Ignatushchenko M, Seki T, Larsson EA, et al. 2013. Monitoring drug target engagement in cells and tissues using the cellular thermal shift assay. *Science* 341:84–87
[31] Jafari R, Almqvist H, Axelsson H, Ignatushchenko M, Lundbäck T, et al. 2014. The cellular thermal shift assay for evaluating drug target interactions in cells. *Nature Protocols* 9:2100–2122
[32] Newman AM, Liu CL, Green MR, Gentles AJ, Feng W, et al. 2015. Robust enumeration of cell subsets from tissue expression profiles. *Nature Methods* 12:453–457
[33] Liao M, Liu Y, Yuan J, Wen Y, Xu G, et al. 2020. Single-cell landscape of bronchoalveolar immune cells in patients with COVID-19. *Nature Medicine* 26:842–844
[34] Delorey TM, Ziegler CGK, Heimberg G, Normand R, Yang Y, et al. 2021. COVID-19 tissue atlases reveal SARS-CoV-2 pathology and cellular targets. *Nature* 595:107–113
[35] Finley D, Bartel B, Varshavsky A. 1989. The tails of ubiquitin precursors are ribosomal proteins whose fusion to ubiquitin facilitates ribosome biogenesis. *Nature* 338:394–401
[36] Vanhaesebroeck B, Guillermet-Guibert J, Graupera M, Bilanges B. 2010. The emerging mechanisms of isoform-specific PI3K signalling. *Nature Reviews Molecular Cell Biology* 11:329–341
[37] Genheden S, Ryde U. 2015. The MM/PBSA and MM/GBSA methods to estimate ligand-binding affinities. *Expert Opinion on Drug Discovery* 10:449–461
[38] Xue C, Yao Q, Gu X, Shi Q, Yuan X, et al. 2023. Evolving cognition of the JAK-STAT signaling pathway: autoimmune disorders and cancer. *Signal Transduction and Targeted Therapy* 8:310
[39] Choby JE, Howard-Anderson J, Weiss DS. 2020. Hypervirulent *Klebsiella pneumoniae* – clinical and molecular perspectives. *Journal of Internal Medicine* 287:283–300
[40] Mu A, Klare WP, Baines SL, Ignatius Pang CN, Guérillot R, et al. 2023. Integrative omics identifies conserved and pathogen-specific responses of sepsis-causing bacteria. *Nature Communications* 14:1530
[41] Vandereyken K, Sifrim A, Thienpont B, Voet T. 2023. Methods and applications for single-cell and spatial multi-omics. *Nature Reviews Genetics* 24:494–515
[42] Baysoy A, Bai Z, Satija R, Fan R. 2023. The technological landscape and applications of single-cell multi-omics. *Nature Reviews Molecular Cell Biology* 24:695–713
[43] Singh P, Gollapalli K, Mangiola S, Schranner D, Yusuf MA, et al. 2023. Taurine deficiency as a driver of aging. *Science* 380:eabn9257
[44] Ye H, Borusak S, Eberl C, Krasenbrink J, Weiss AS, et al. 2023. Ecophysiology and interactions of a taurine-respiring bacterium in the mouse gut. *Nature Communications* 14:5533
[45] Xiao Z, Jiang S, Fu S, Zhang X, Qi X, et al. 2025. Unveiling the therapeutic mechanism of *Epimedium herba* on prostate cancer through network pharmacology and experimental validation. *Chinese Journal of Natural Medicines* 23:100016
[46] Racz LZ, Racz CP, Pop LC, Tomoaia G, Mocanu A, et al. 2022. Strategies for improving bioavailability, bioactivity, and physical-chemical behavior of curcumin. *Molecules* 27:6854
[47] Suresh MV, Francis S, Aktay S, Kralovich G, Raghavendran K. 2023. Therapeutic potential of curcumin in ARDS and COVID-19. *Clinical and Experimental Pharmacology and Physiology* 50:267–276
[48] Jiang L, Guo P, Ju J, Zhu X, Wu S, et al. 2023. Inhalation of L-arginine-modified liposomes targeting M1 macrophages to enhance curcumin therapeutic efficacy in ALI. *European Journal of Pharmaceutics and Biopharmaceutics* 182:21–31
[49] Peng T, Rao J, Zhang T, Wang Y, Li N, et al. 2023. Elucidation of the relationship between evodiamine-induced liver injury and CYP3A4-mediated metabolic activation by UPLC-MS/MS analysis. *Analytical and Bioanalytical Chemistry* 415:5619–5635
[50] Lin L, Liu Y, Tang R, Ding S, Lin H, et al. 2024. Evodiamine: an extremely potential drug development candidate of alkaloids from *Evodia rutaecarpa*. *International Journal of Nanomedicine* 19:9843–9870
[51] Tadtong S, Atiwanitchakul K, Moohammad M, Chittasupho C, Tangjidapichai C, et al. 2026. Combined anti-inflammatory effects of curcumin and evodiamine: *in vitro* synergy, docking, and molecular orbital insights. *International Journal of Molecular Sciences* 27:3834

Copyright: © 2026 by the author(s). Published by Maximum Academic Press on behalf of China Pharmaceutical University. This article is an open access article distributed under Creative Commons Attribution License (CC BY 4.0), visit https://creativecommons.org/licenses/by/4.0/.